Mid-mantle anisotropy in subduction zones and deep water transport

Andy Nowacki[1], J.-Michael Kendall[1], James Wookey[1] and Asher Pemberton[1]

Abstract. The Earth's transition zone has until recently been assumed to be seismically isotropic. Increasingly, however, evidence suggests that ordering of material over seismic wavelengths occurs there, but it is unclear what causes this. We use the method of source-side shear wave splitting to examine the anisotropy surrounding earthquakes deeper than 200 km in slabs around the globe. We find significant amounts of splitting ($\leq$ 2.4 s), confirming that the transition zone is anisotropic here. However, there is no decrease in the amount of splitting with depth, as would be the case for a metastable tongue of olivine which thins with depth, suggesting this is not the cause. The amount of splitting does not appear to be consistent with processes in the ambient mantle, such as lattice preferred orientation development in wadsleyite, ringwoodite or $MgSiO_3$-perovskite. We invert for the orientation of several mechanisms—subject to uncertainties in mineralogy and deformation—and the best fit is given by up-dip flattening in a style of anisotropy common to hydrous phases and layered inclusions. We suggest that highly anisotropic hydrous phases or hydrated layering is a likely cause of anisotropy within the slab, implying significant water transport from the surface down to at least 660 km depth.

1. Introduction

The mechanisms for the transport of material from the Earth's surface to its deep interior by subduction are of great interest to all aspects of Earth science. However, placing constraints on the chemistry and dynamics of this material—transported in the form of slabs—is difficult. There is still uncertainty about the eventual fate of slabs, with some appearing to stall at the base of the mantle transition zone (TZ), and others seemingly travelling through to the lower mantle (LM) without hindrance [*Kárason and van der Hilst*, 2000]. Much debate has centred on the degree to which water is cycled into the deep Earth, but despite growing geochemical and geophysical evidence [*Hirschmann*, 2006], quantifying this is still challenging. Observing anisotropy in deep slabs may be able to help resolve some of these questions because it provides information about deformation and even phase stability, which possibly also places constraints on chemistry, including water content.

Traditionally it has been assumed that the TZ is isotropic, as the mechanisms for anisotropy in this region are not readily clear. Ringwoodite, present between the 520 km-deep discontinuity and the 660 km discontinuity (the '520' and '660', respectively), is nearly isotropic [*Li et al.*, 2006]. Wadsleyite, the dominant mineral between the 410 km discontinuity ('410') and the 520, is more anisotropic, and early experiments hinted it may form a lattice-preferred orientation (LPO) [*Thurel et al.*, 2003; *Thurel and Cordier*, 2003; *Tommasi*, 2004]. However more recent studies have indicated that the mineral has slip systems of similar strength and therefore does not readily form an LPO [*Ohuchi et al.*, 2014]. Deeper still, magnesium silicate-perovskite (pv) in the uppermost lower-mantle (ULM) is highly anisotropic and may develop a significant LPO if large strains exist near the 660 [*Cordier et al.*, 2004; *Wenk et al.*, 2004; *Mainprice et al.*, 2008]. Slab mineralogy at these depths is more uncertain. Olivine may be meta-stable in narrowing regions of slab cores [*Kirby et al.*, 1996], water may lead to significant amounts of a hydrous phases in the subducted lithosphere [*Ohtani*, 2005], and akimotoite may exist in the high-P, low-T slab core [*Liu*, 1976; *Akaogi et al.*, 2002].

Despite the unclear cause of TZ anisotropy, there is a growing body of evidence for the presence of seismic anisotropy in this region. Studies of normal modes and surface waves have shown variable degrees of anisotropy in the TZ, and even in the ULM [e.g., *Montagner and Kennett*, 1996; *Trampert and van Heijst*, 2002; *Yuan and Beghein*, 2013]. Observations of two independent shear waves offers better lateral resolution of this anisotropy, but a challenge lies in unravelling the competing effects of near-receiver anisotropy in the uppermost mantle. The tendency of slab minerals to develop an LPO is not well known, but the effects of anisotropy in this area on seismic body waves can be significant [*Kendall and Thomson*, 1993]. Furthermore, seismic sources in subducting slabs are good probes of anisotropy beyond the slab in the TZ [*Tong et al.*, 1994; *Fouch and Fischer*, 1996; *Chen and Brudzinksi*, 2003; *Foley and Long*, 2011; *Lynner and Long*, 2014] and the ULM [*Wookey et al.*, 2002; *Wookey and Kendall*, 2004; *Nippress et al.*, 2004]. If near-receiver anisotropy is well characterised it can be used as a correction to estimate shear-wave splitting near the source region [*Wookey et al.*, 2005; *Nowacki et al.*, 2010, 2012]. Here we use source-side shear-wave splitting to interrogate anisotropy in the TZ and ULM in regions of subduction. We show that the amount of splitting is relatively larger than previously expected (up to 2.4 s), and that it is unlikely that the cause is the alignment of mineral grains in the ambient mid- or lower mantle. Instead, a highly anisotropic region within the slab is our preferred explanation, suggesting hydrous phases are carried to at least the bottom of the TZ.

2. Data and methods

2.1. Data

In order to investigate anisotropy beneath deep slab earthquakes, we measure shear wave splitting in the S

[1]School of Earth Sciences, University of Bristol, Bristol, UK

Copyright 2015 by the American Geophysical Union.

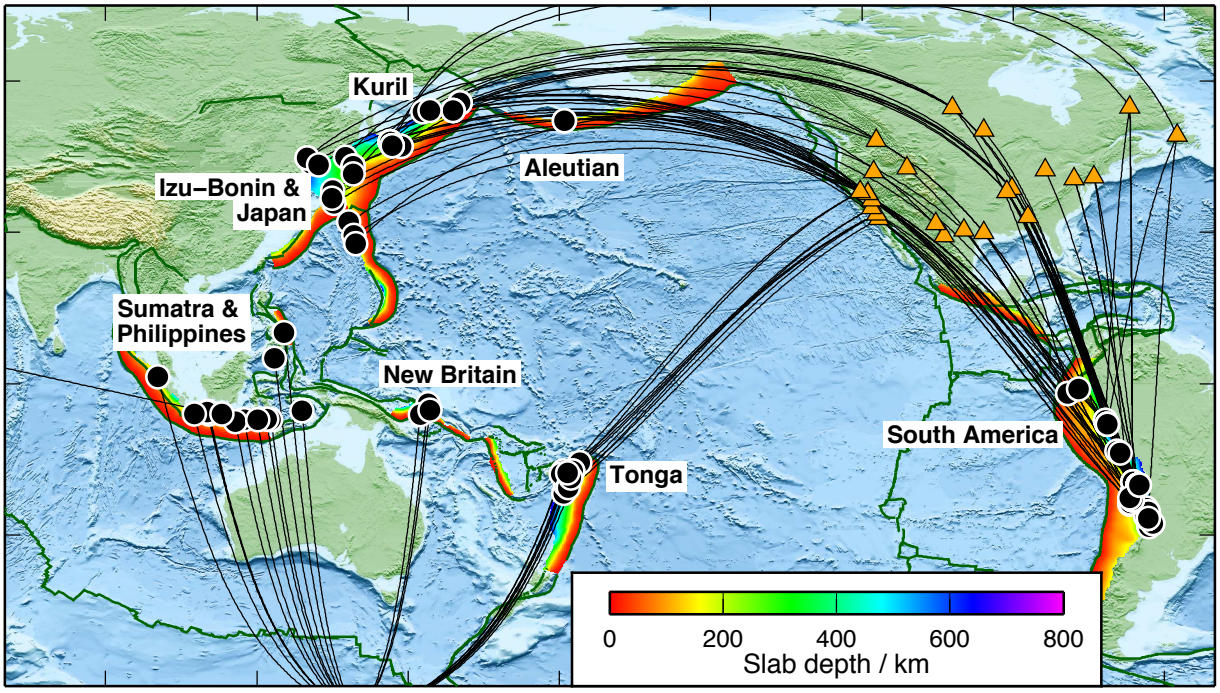

Figure 1. Location of earthquakes (black circles) and stations (orange triangles) used in this study, plotted over contours of slab depths given by *Hayes et al.* [2012], shown by colour (see scale). Subduction regions as discussed in the text are labelled. Raypaths between events and receivers are shown with black lines. Stations DRV (Antarctica) and FURI (Ethiopia) are not shown.

phase in the epicentral distance range $55^\circ \leq \Delta \leq 82^\circ$ for events deeper than 200 km with magnitude $M > 4.5$. This distance range prevents S waves from interacting with the lowermost ∼300 km of the mantle, which is also anisotropic. Locations are taken from the International Seismological Centre (ISC) where locations exist, and otherwise the National Earthquake Information Center (NEIC) of the United States Geological Survey (USGS). Figure 1 shows the distribution of events in this study. Moment tensors for each event were taken from the Global CMT project (http://www.globalcmt.org).

2.2. Source-side shear wave splitting

Details of our method are given by *Nowacki et al.* [2012], however we describe briefly the method and quality criteria below.

We wish to determine the shear wave splitting caused in the vicinity of the earthquake in the TZ and uppermost LM. According to several global studies of radial anisotropy [*Kustowski et al.*, 2008; *Montagner and Kennett*, 1996; *Panning and Romanowicz*, 2006, 2004], the strength of anisotropy in the majority of the LM is very small. Hence we make here the common assumption that no shear wave splitting is accrued in most of the lower mantle. In order to measure splitting near the source, therefore, we must remove the effects of anisotropy near the receiver. We do this by using receivers where the sub-station splitting has been very well characterised using SKS splitting measurements in previous studies [J.O.S. Hammond, pers. comm.; *Ayele et al.*, 2004; *Barruol et al.*, 1997; *Barruol and Hoffmann*, 1999; *Fouch et al.*, 2000; *Liu*, 2009; *Niu and Perez*, 2004]. Any variation in the SKS splitting parameters with backazimuth betrays the presence of complex, dipping or heterogeneous anisotropy in the UM beneath the station, so we use only stations where splitting parameters are invariant with backazimuth and where good backazimuthal coverage is available. The absence of any backazimuthal variation also precludes any significant splitting in SKS from D″ [*Hall et al.*, 2004], which though known to be azimuthally anisotropic [*Nowacki et al.*, 2011] does not appear to be responsible for significant splitting in SKS waves [*Niu and Perez*, 2004; *Restivo and Helffrich*, 2006]. We also avoid stations above subduction zones, because of the potential for TZ anisotropy to be present beneath the receiver in these locations, as well as the source, which would increase the likelihood that our receiver correction is not complete. (Details of the corrections used for each station are in the supplementary information.) We finally avoid stations which appear to exhibit no splitting (in comparison to *Foley and Long* [2011] and *Lynner and Long* [2014]) because it seems very likely that these stations sit atop regions where multiple layers or domains of anisotropy cancel each other out, rather than there is complete isotropy between the lower mantle and the surface along the SKS paths which are used to measure splitting.

The SKS splitting measurements are assumed to be a good approximation to the splitting experienced by direct S waves, as they share very similar paths in the upper mantle (Figure 3a). We measure the splitting in the direct S waves and remove the splitting measured in SKS, hence the remaining splitting should be caused by anisotropy in regions where the paths differ. This is mostly in the region near the earthquake. However, any difference in splitting between S and SKS—for example, due to unaccounted-for TZ anisotropy beneath the receiver—will also affect our observations. We assume this is not the case from here onwards.

We mainly discuss our results in terms of the ray-frame fast orientation, ϕ' (Figure 3b). This describes the orientation of the fast shear wave with respect to the Earth radial direction (equivalently, the sagittal plane) when looking along the ray from source to receiver. For near-vertical rays at the receiver, $\phi' = \beta - \phi$, where β is the backazimuth at the receiver and ϕ is the orientation of the fast shear wave measured at the surface, given as an azimuth from local north towards east. (Using a fully slowness-dependent expression gives values different only by a few degrees for the distance ranges we use, which is typically within the uncertainty of

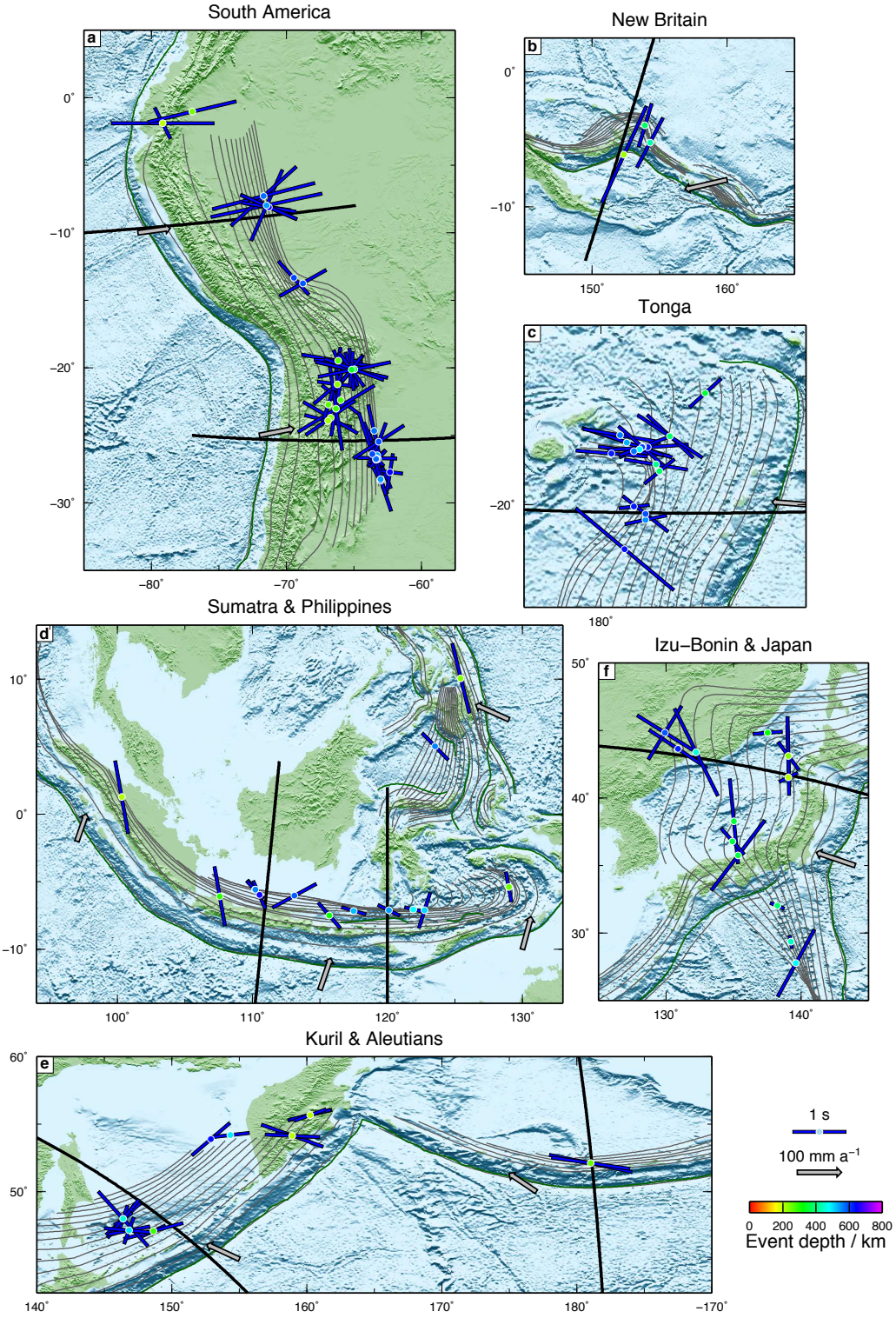

Figure 2. Source-side shear wave splitting results for earthquakes beneath (a) South America, (b) New Britain, (c) Tonga, (d) Sumatra and Philippines, (e) Kuril and Aleutians and (f) Izu–Bonin and Japan. The orientation of the bars shows the orientation of the fast shear wave projected to the source, ϕ'', and the length of the bars is proportional to the delay time, δt, as shown in the legend. Coloured circles show the depth of the earthquake as indicated in the legend, and grey arrows show the convergence rate given by NUVEL-1A [*DeMets et al.*, 1994] at selected points along the subduction interfaces. Thick black lines show line of sections in Figure 5.

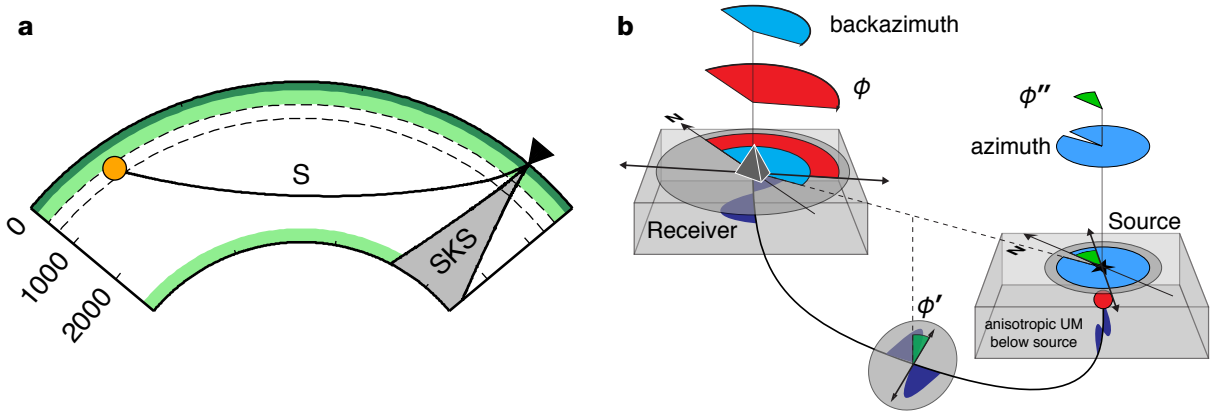

Figure 3. Experimental setup. (a) Mantle section showing the ray path of the S wave from source region (orange circle) to receiver at surface (inverted triangle). Grey shaded region shows the path of SKS across all backazimuths. Green regions are parts of the mantle generally known to be anisotropic. (b) Explanation of the fast shear wave orientation in the receiver (ϕ), ray (ϕ') and source (ϕ'') frames.

the splitting measurement.) In this notation, horizontally polarised S waves (SH) corresponds to $\phi' = 90°$ and vertically polarised (SV), $\phi' = 0°$.

We also discuss results in the source-frame orientation, ϕ'', where ϕ is projected back to the surface above the source; this is given by $\phi'' = \alpha + \beta - \phi$, where α is the azimuth from the source to the receiver.

Finally, we introduce the slab reference frame (section 4). This relates the orientation in the ray frame into the local plane of the slab as defined by seismicity, and requires knowledge of the local strike and dip of the slab.

3. Results

In total, 130 shear wave splitting measurements could be made which met our criteria, using 80 events with magnitude range $4.9 \leq M_b \leq 7.3$ and maximum depth 648 km. Although 13 clear observations of no splitting ('nulls') were made, about half of these had large uncertainties on ϕ. Consequently, because of the limited number of them, we do not consider the null observations further. We subdivide our analyses of the results into sections by subduction zone.

3.1. South America

A total of 59 individual measurements were made beneath South America, from 27 events. When considered in the source frame (Figure 2a), ϕ'' is dominantly east–west for events to the north, and north–south for southern events (more than 25° south), however the pattern is complicated. In the ray frame, this pattern translates to fast shear waves inclined at about 30° to the horizontal in the north (Figure 5, 'South America 1'), and vertical in the south (Figure 5 'South America 2'), with some variation of splitting parameters with azimuth.

3.2. Tonga

In Tonga (Figure 2c), ϕ'' shows a strong east–west trend (approximately parallel to the subduction direction), corresponding to an SH-fast ($\phi' \approx 90°$) pattern (Figure 5 'Tonga'). This is in contrast to the pattern seen by *Foley and Long* [2011], who observe fast orientations more closely parallel to the trench.

3.3. Japan, Izu-Bonin, Kuril and Aleutians

In these regions we were able to make fewer observations, however there are still some consistent patterns. In the Izu–Bonin and Japan region (Figure 2f), the range of δt is large (0.3 to 1.3 s), showing larger splitting to the northwest in the Japanese slab. No clear trend at the surface is present, but ϕ' trends close to SH in the ray frame. Our results are similar to those given by *Lynner and Long* [2014].

Further northeast, two clusters of results in the Kuril slab (Figure 2e) generally show trench-parallel (southwest) or trench-oblique (northeast) fast orientations in the receiver frame. The two groups lead to fast orientations in the ray frame of either $\sim -10°$ or $\sim 45°$, which seems (Figure 5 'Kuril') to be azimuth-dependent, with the near-SV orientations being associated with smaller azimuths (paths bend-

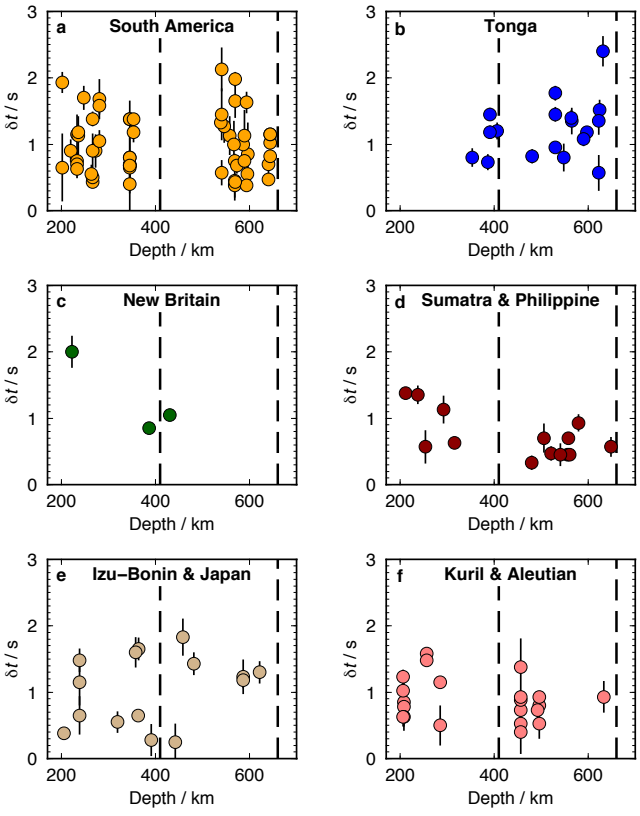

Figure 4. Amount of splitting, δt, versus depth for all events, shown by region. Error bars show 2σ uncertainty in the splitting measurement.

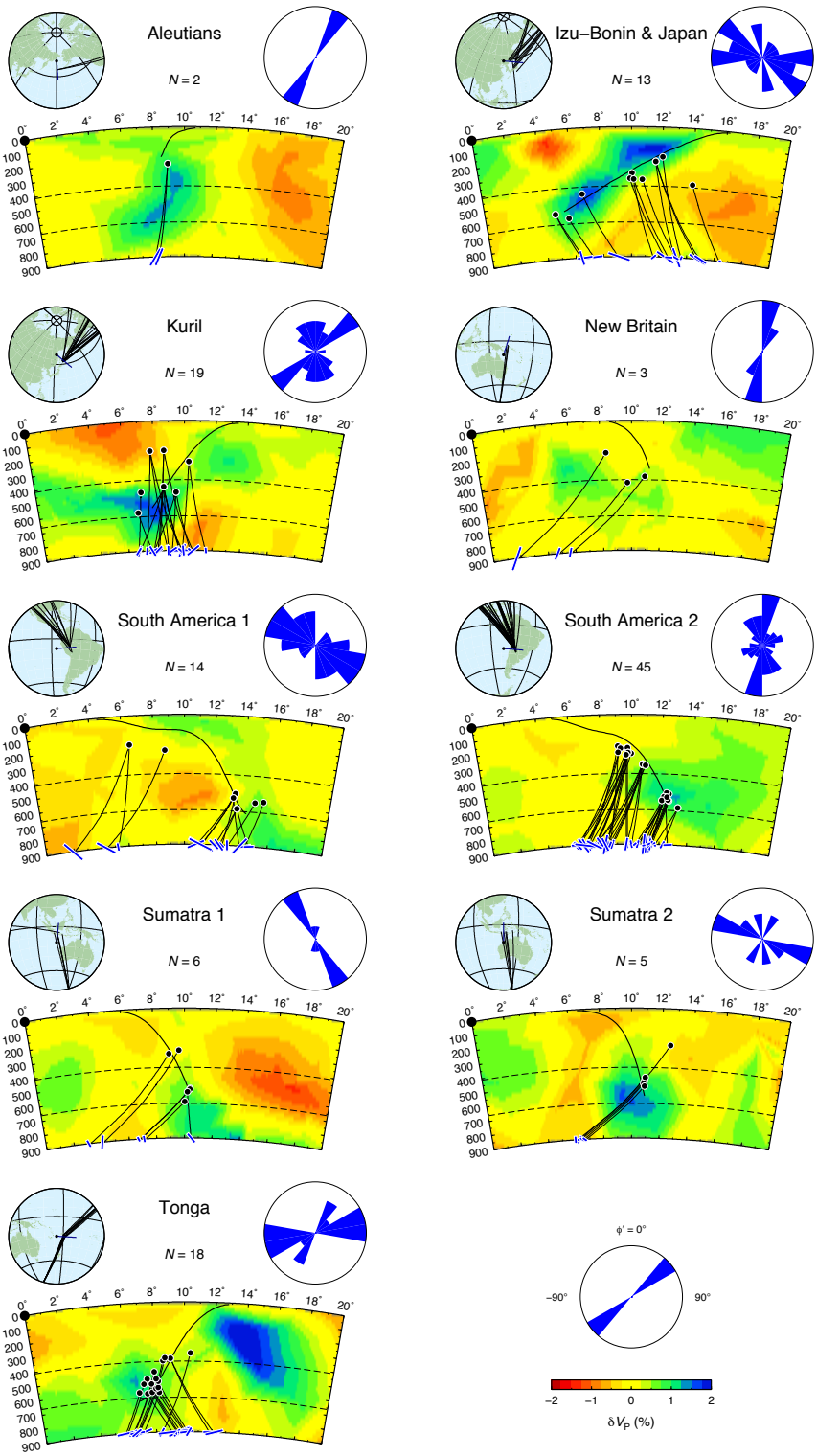

Figure 5. Sections through each region in this study, showing shear wave splitting measurements in the ray frame. Map (upper left) shows the start point of section with the black circle and the line of section with thick line. Raypaths to stations are shown with thin lines. Cross sections (centre) show the slab profile along the section as given by the slab1.0 model [*Hayes et al.*, 2012] with the thick black line. Small black circles show the event locations projected onto the section; in some cases the events project away from the slab surface for the specific profile. Thin black lines show the ray paths from the earthquake to the receiver projected onto the section; hence near-vertical rays travel nearly perpendicular to the section. Blue bars at the base of the section show the ray-frame splitting parameters. Length corresponds to delay time, δt and angle clockwise from the vertical shows the value of ϕ'. The polar histograms (upper right) show the distribution of ray-frame fast orientations for the section, with $phi' = 0$ at the top, increasing clockwise, as indicated in the explanatory diagram, bottom right. Colour in the section shows perturbation from the reference model in P velocity for the tomographic model PRI-P05 [*Montelli et al.*, 2004], as indicated in the scale, bottom right. The number of measurements is shown by N.

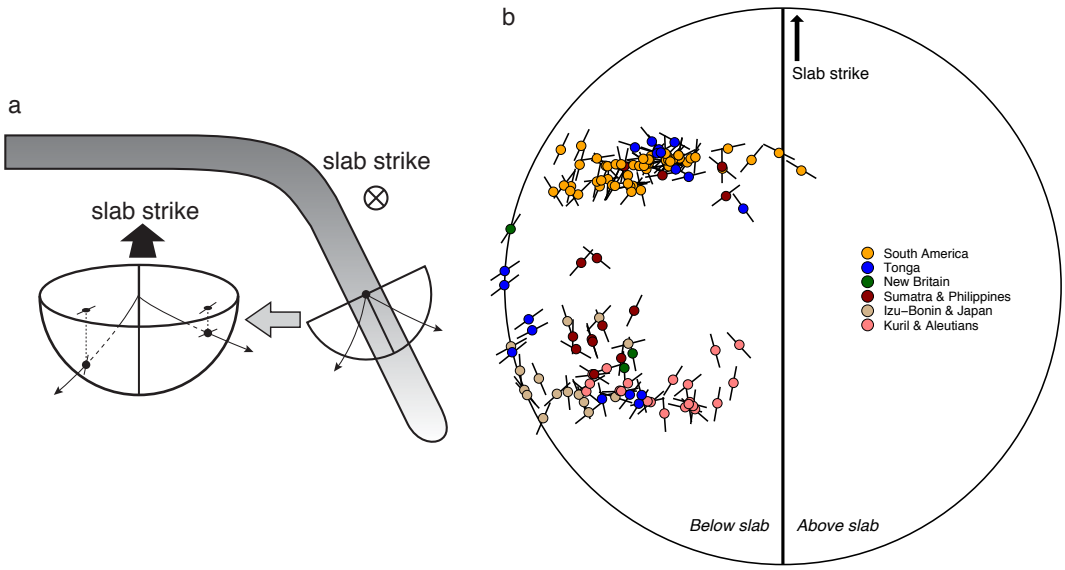

Figure 6. All source-side shear wave splitting results in the slab frame. (a) Explanation of the lower hemisphere figure in b. (b) Equal-area lower hemisphere projection of shear wave splitting results of all events in the slab frame (see text). Each region is colour coded, as shown in the legend. Some data points for Tonga leave the slab region at a few degrees more than 90° to the slab normal, and have been plotted on the edge of the lower hemisphere.

ing left on the section), and values of ϕ' near 45° leaving at larger azimuths.

Two relatively shallow events in the Aleutian arc (Figure 2e) show trench-parallel ϕ'' and $\phi' \approx 25°$, $\delta t = 1.5$ s.

3.4. Sumatra, Philippines, New Britain

Along the Sumatran slab (Figure 2d), fast orientations seem to vary with longitude, with ϕ'' in the far west being consistently oblique to the trench, in a similar way to that observed by *Di Leo et al.* [2012] and *Lynner and Long* [2014]. This region is also perhaps the only one where δt decreases noticeably with event depth (Figure 4). When considering the ray frame orientation (Figure 5, 'Sumatra 1' and 'Sumatra 2'), there is also a clear east–west difference. Events in the west ('Sumatra 1') have ϕ' near to vertical, whereas in the East ('Sumatra 2') the major trend is closer to SH. The single observations possible beneath the Philippine and Sangihe subduction zones show a mixture of trench-parallel and -oblique fast orientations.

Beneath New Britain (Figure 2b), ϕ'' is consistently trench-normal, but oblique to the subduction direction, whilst ϕ' (Figure 5 'New Britain') is ∼0°.

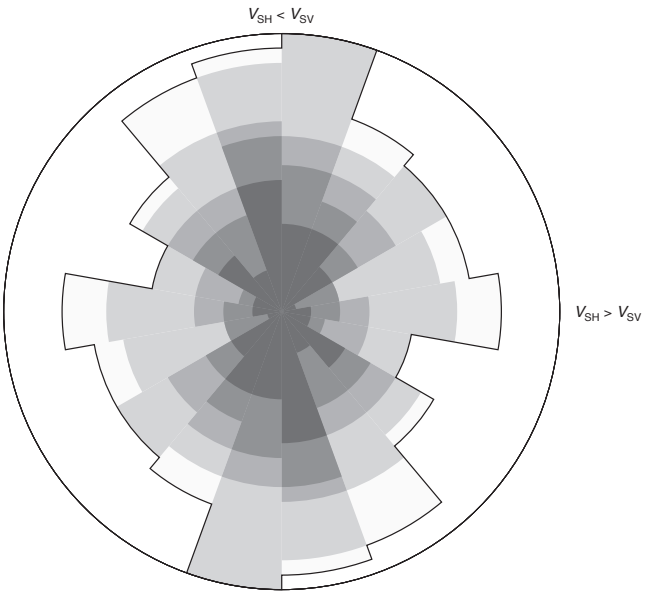

Figure 7. Polar histogram of ϕ' for all events in this study for bins of 20°. Each bar represents the total number of events, and each separately coloured stacked bar shows the frequency within a given depth range. Darkest shade shows range 200–300 km, lightest shows 600+ km. No single direction dominates for the global set.

3.5. Global patterns and strength of anisotropy

In the global data set, there is no trend of the amount of splitting or fast orientation with ray path distance between the event and station (for linear fits weighted by the errors in δt, the squared Pearson correlation coefficient $R^2 < 0.01$ for all data), nor is there any apparent relationship between path length and ϕ'. Equally, there is no clear dominant global value of ϕ' (Figure 7).

The global mean δt is (1.0 ± 0.4) s (1 s.d.), similar to that observed in SKS splitting studies of the UM. At 650 km deep, a layer 100 km thick requires shear wave anisotropy of approximately 6 %; a 50 km layer requires 11 % anisotropy; and equivalently a 200 km layer requires 3 %.

4. Interpretation and implications

In order to interpret the results, it is important to consider the location and mechanism of anisotropy around these deep slabs. Therefore, we consider the results in a number of different reference frames:

1. the source frame (considering ϕ'');
2. the global frame (considering ϕ'); and
3. the slab frame.

The first two have been previously described. In the slab frame, fast orientations are related to the approximate plane

which describes the slab in the transition zone, based on seismicity in the slab [*Hayes et al.*, 2012]. To do this, we use the event locations and ray take-off angles calculated at 660 km depth in the AK135 model [*Kennett et al.*, 1995] to rotate the fast orientations such that the new vertical direction is parallel to the slab up-dip direction, and the ray's azimuth is measured clockwise from the slab strike, where the strike is 90° anti-clockwise from the downdip direction when looking from above. The new fast orientations are therefore not necessarily intuitively related to those in the source or global frame. We plot these orientations on an equal-area lower-hemisphere projection (Figure 6). It is notable when doing so that only one or two ray paths from the event to the receiver travel in the region above the slab for the entire dataset: instead, most leave the slab in the forearc direction. This means that in this study we have no sensitivity to anisotropy above the slab. This is a result simply of the location of deep subduction zones and our receivers.

It is difficult to qualitatively assess whether there is any consistent pattern between or within the results for each region by simple inspection, so instead we consider some first-order anisotropic cases which may fit the data and offer insight into the causes of anisotropy in these regions below.

4.1. Location of anisotropy

If the shear wave splitting we observe were mainly due to anisotropy in the slab, there should be a difference in δt between rays travelling along the slab, and those quickly leaving in the back-arc direction. As shown in Figure 8, there is no clear trend of larger splitting for paths spending more time within the slab (near the centre line) versus those where rays quickly leave the slab behind the slab (to the left). In fact, it appears the opposite is true, with δt up to 2 s for paths normal to the up-dip direction. This suggests either that the anisotropy is confined to a strong region immediately surrounding the event, or alternatively it is not confined to the slab at all. A third explanation may be that the style of anisotropy means that relatively little splitting is produced in rays which travel along the slab, even though anisotropy is confined to the slab region.

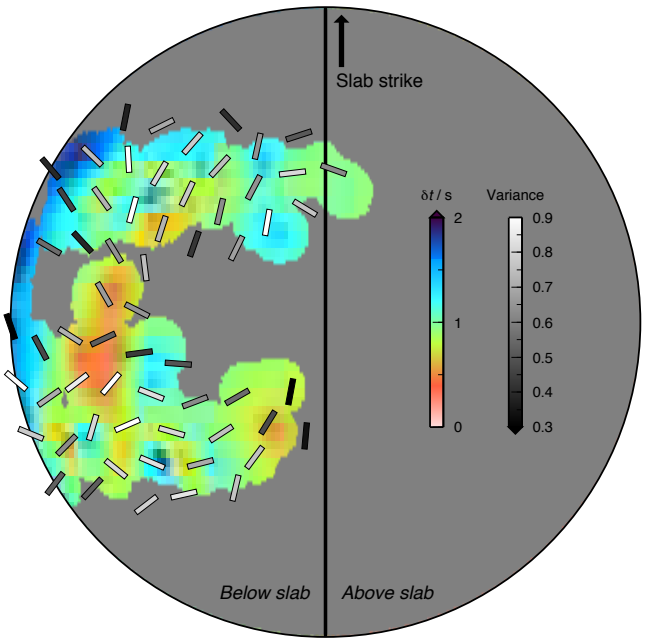

Figure 8. Smoothed average of all results in the slab reference frame (Figure 6; lower hemisphere equal area projection) for all regions. Amount of shear wave splitting, δt is shown by colour. A running average has been applied by fitting with surface splines under tension [*Smith and Wessel*, 1990]. Fast orientations have been circularly averaged within a radius of 15° and plotted spaced evenly at 10° intervals on the sphere. Dark bars indicate orientations which are most consistent (have the smallest circular variance); lighter colours show where there is more scatter within the bin. Grey areas show where there are no data.

Another important observation as shown in Figure 4 is that there is no clear trend of variation of δt with depth, either within an individual region or globally. This suggests that the anisotropy is not constrained to the upper parts of the TZ, but instead may be focussed near the events, or at or below the base of the TZ. Notably, even events at ∼650 km beneath South America exhibit significant splitting (∼1 s). Hence the most likely location for the anisotropy is at the top of the lower mantle, or within the slab itself.

We note also that there is no clear variation within the whole dataset or individual regions for a change of slab-frame fast orientation with depth.

4.2. Possible causes of anisotropy

There are a number of potential causes for anisotropy in the sub-slab mantle in the TZ and ULM. Primarily, it may be due to the alignment of anisotropic mineral grains (lattice-preferred orientation, LPO), potentially caused by the motion of dislocations in the crystal lattices due to deformation. If this is the case, there are several candidate phases which may be the cause. The upper and lower TZ are dominated by wadsleyite and ringwoodite (∼60 % by volume in a pyrolite composition), respectively, with garnet and some $CaSiO_3$-perovskite ($\leq$10 %) [*Irifune and Tsuchiya*, 2007]. We do not consider Ca-perovskite further because of its low abundance. Although it has been shown to form an LPO under strain [*Kavner*, 2003; *Wenk et al.*, 2004], single-crystal ringwoodite is believed to be very weakly anisotropic [<1 % shear wave anisotropy; *Higo et al.*, 2006; *Li et al.*, 2006], even in the hydrous state, so it does not seem possible as a causative mechanism: even with perfect alignment of this phase, to produce 1 s of shear wave splitting would require a layer over 2000 km thick. Hence we rule out LPO in ringwoodite from further discussion. Wadsleyite, on the other hand, is moderately anisotropic [*Zha et al.*, 1997], but there is still uncertainty regarding its deformation mechanism and it appears that though it may form a weak LPO, this decreases with water content [*Ohuchi et al.*, 2014].

Other phases present in the lower TZ of the surrounding mantle could instead be a cause. It is possible that the tetragonal majorite phase ($Mg_3(MgSi)Si_3O_{12}$) is stable at these conditions [*Yu et al.*, 2011], and would make up ∼30 % of the mantle, however it is even less anisotropic than ringwoodite [*Murakami et al.*, 2008]. We also exclude majorite on this basis.

Akimotoite ($MgSiO_3$ in the ilmenite form) may be present in the lower TZ and ULM [*Akaogi et al.*, 2002], but it is as yet uncertain to what extent. However, it is extremely anisotropic [up to ∼35 % in certain directions; *Li et al.*, 2009; *Zhang et al.*, 2005] and is known to form an LPO under TZ conditions [*Shiraishi et al.*, 2008].

Dense hydrous magnesium silicate phases (DHMSs, also known as the 'alphabet phases') such as phases D [*Liu*, 1987], H [*Nishi et al.*, 2014] and superhydrous B have been observed experimentally in pyrolite compositions with a few percent water by weight at TZ conditions [for reviews, see *Ohtani*, 2005; *Faccenda*, 2014]. These are often very anisotropic (up to ∼20 %) and hence could give splitting comparable to our observations over short distances or with low abundances.

If the anisotropy is present instead around the slab in the lower mantle, then it might be due to LPO in $MgSiO_3$-perovskite (pv, now called bridgmanite) or (Mg,Fe)O, the dominant phases present at LM conditions in pyrolite. It is still uncertain as to the likely extent of partitioning of strain between these phases, but because pv is likely to make up about 80% of the mantle, we do not consider (Mg,Fe)O. Experiments show that pv forms an LPO at high P–T conditions [*Cordier et al.*, 2004; *Wenk et al.*, 2004], though *Mainprice et al.* [2008] suggest that anisotropy in pv decreases with pressure and temperature and would lead to <2 % shear wave anisotropy.

A final explanation which cannot be ruled out with these data is extrinsic anisotropy due to the periodic alignment of pockets of material with contrasting seismic properties (shape-preferred orientation or SPO). Basic modelling using effective medium theory [e.g., *Tandon and Weng*, 1984] shows that elliptical inclusions much shorter in one dimension than the other two ('smarties') necessarily lead to the pattern we observe in Figure 8: large shear wave splitting at the edges with low splitting nearer to the centre of the plot. The pattern of fast orientations is also matched with this situation (Figure 6). Note that periodic layering would cause the same features. A possible cause for this could be the trenchward-dipping faults developed at the outer rise during subduction [*Masson*, 1991], which may be responsible for significant alteration of the lithospheric mantle [e.g., *Ranero and Sallarès*, 2004].

4.3. Inversion for orientation of candidate phases

In order to more quantitatively interpret our results, we take some of the possible causes of anisotropy in the lower TZ and invert for the orientation of each assumed mechanism. In order to represent a range of possible textures, whilst also recognising the limited resolving power of the dataset, we fix several parameters and invert only for the orientation and layer thickness (which trades off with strength or phase proportion in an isotropic aggregate). We can reject mechanisms which require an unrealistic amount of the phase.

Throughout this modelling, it is important to note that our current lack of knowledge requires us to make many assumptions. First of all, the single-crystal elastic constants for TZ and ULM phases are still somewhat uncertain; furthermore, few experiments have been performed studying LPO in them, hence deformation mechanisms are still relatively poorly known, especially concerning the effects of temperature, pressure and chemistry. Secondly, with these uncertainties in mind, we assume very simple, uniform (planar) deformation geometries in or around the slab, which are likely in reality to be more complex. Instead, we make unavoidable assumptions and appeal to the simplest explanation which best fits the data.

We first consider elliptical anisotropy (Figure 11a). This is a special case of hexagonal symmetry [*Thomsen*, 1986] where fast orientations are always within the plane normal to the rotational symmetry axis. Using Thomsen's notation (see *Mainprice* [2007] for a summary), we fix in the slab frame V_{SV}, V_{PV} and ρ to the values of AK135 at 670 km depth and set $\delta = \gamma = 0.1$. (We also set $\epsilon = 0.1$ but have no sensitivity to ϵ because we are only considering shear waves.) Note that in this context SH and SV are related to the axis of symmetry, and not the Earth radial direction. Note also that we are insensitive to the isotropic average velocities, because we are inverting shear wave splitting observations, hence we may choose to take values from any depth. This type of anisotropy can be considered the most simplistic case, and corresponds to the form of transverse isotropy (TI) most commonly assumed in global S-wave inversions for radial anisotropy (where the parameters ϕ and $\eta \approx 1$). Because the axis of rotational symmetry is generally tilted, it is often called tilted transverse isotropy (TTI). Note that it does not relate to the type of anisotropy expected from periodic layering of material or elliptical inclusions, which would appear much more similar to the hexagonal phases we consider next.

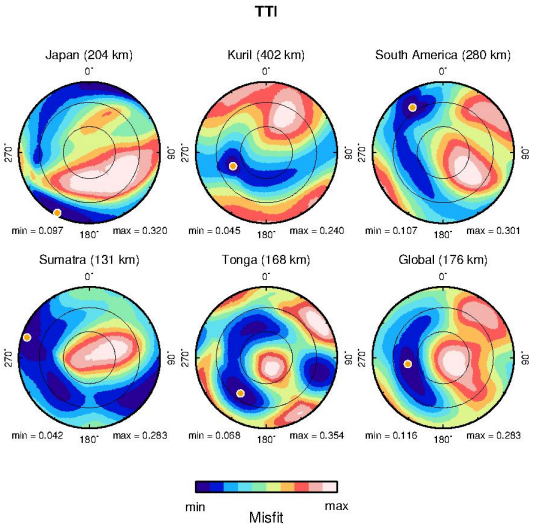

Figure 9. Misfit surfaces for each region and the global dataset (all regions combined) from the inversion for the orientation of the rotational symmetry axis of TTI. Lower hemisphere, equal area projections are in the slab frame (as in Figure 6), and show the misfit per observation, with black circles spaced at 30° of incidence angle. Colour bar at bottom goes from minimum (blue) to maximum (pink) misfit for each region, with these values given below each hemisphere. Distance in brackets gives the required thickness of a single layer required to fit the observations in δt. Orange circles show the minimum misfit orientation.

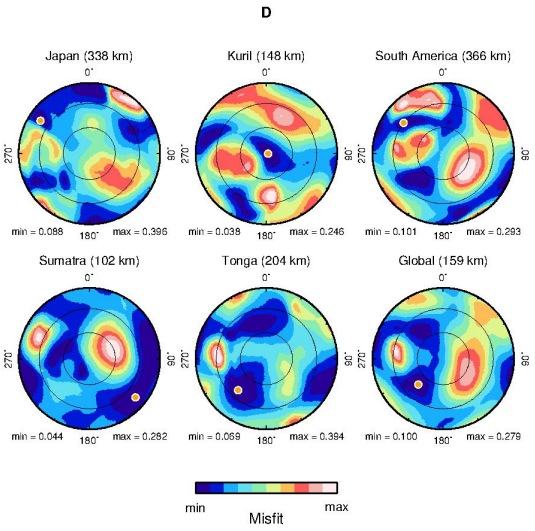

Figure 10. Misfit surfaces for deformed phase D. Features as for Figure 9.

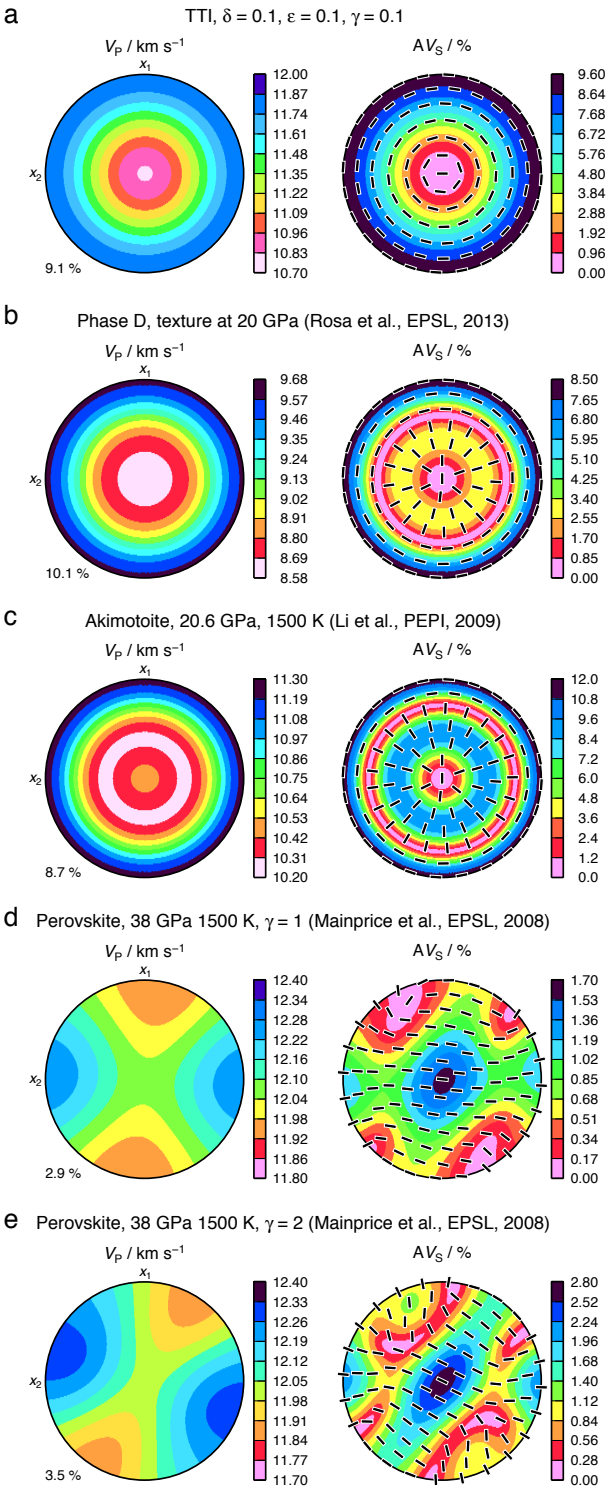

Figure 11. Phase velocity surfaces (equal area upper hemisphere) for the sets of elastic constants for which we invert their orientation. Left hand plots show P wave velocity as a function of direction. Right hand plots show shear wave anisotropy (%) with colour, and the orientation of the fast shear wave as black bars. (a) TTI. For phase D (b), we combine elastic constants at 0 GPa and 300 K with the textures at 20 GPa. For akimotoite (c), constants are averaged about the [0001] axis (x_3 direction). For pv (d and e), the shear direction in the calculation is $-x_2$, and the shear plane is perpendicular to x_1.

For phase D (Figure 11b), we use the single-crystal elastic constants from *Rosa et al.* [2012] and combine them using the ODFs found by *Rosa et al.* [2013] for the pure Mg end-member at 19.5 GPa in their deformation experiments. We additionally impose rotational symmetry about the deformation axis because the textures are very close to being symmetric in any case, and this allows us to interpret a single compressional direction.

Note that for akimotoite and phase D, the style of anisotropy produced is essentially the same as that created

by aligned inclusions, such as would be the case for the hydrated lithospheric faulting hypothesis. Many parameters are involved in creating a set of elastic constants (including whether the inclusions themselves are anisotropic) for the aligned inclusions case, and the choice of many of those are somewhat arbitrary. Hence we elect to simply interpret the axial compressions axes in the akimotoite and phase D inversions as being the same as the axis of rotational symmetry for a set of aligned planes or flattened ellipsoidal inclusions.

We next take the constants of akimotoite from *Li et al.* [2009], and—to simulate basal slip during compression [*Shiraishi et al.*, 2008]—we form a rotational average about the [0001] axis and combine the constants using Voigt–Reuss–Hill averaging (Figure 11c).

Finally, we consider two cases of textured pv at 38 GPa and 1500 K as computed by *Mainprice et al.* [2008], for shear strains of 1 and 2 (Figures 11d and 11e; respectively 'pv1' and 'pv2'). We use the elastic constants and allow the distance over which splitting is accrued in the inversion to vary freely.

During the grid search inversion, we rotate the elastic constants to all unique orientations (the degeneracy of which is determined by the crystal symmetry) by rotation about the principal cartesian directions in the slab frame, and compute the misfit between the observed shear wave splitting, and that calculated by using the phase velocities in the corresponding direction within the candidate constants. We use the 'λ_2S splitting misfit' as implemented in the MSAT toolkit [*Walker and Wookey*, 2012], which takes into account the frequency and source polarisation of the shear waves, and hence the characteristic uncertainties which arise when using the small-eigenvalue minimisation scheme as we do here. (See Appendix A.) We use only regions which have at least 12 measurements, as using too few leads to a very large range of orientations which can fit the data and little insight can be gathered in these cases. This means that alongside the global dataset, Japan, Kuril, South America, Sumatra and Tonga are considered further.

The results are shown in Figures 9–12. For the hexagonally-symmetric phases (akimotoite, D and TTI), we show the misfit associated with the orientation of the axis of rotational symmetry in the slab frame. For the perovskite phases, we show the misfit in terms of the orientation of the shear plane, and the shear direction, but only for the best-fitting 0.1 % of orientations. We also show the best-fitting thickness of the layer above each hemisphere. In some cases (e.g., Kuril for TTI or Japan for pv1) there is a single well-constrained minimum. In general, however, there is more than one minimum, which reflects both the limited spherical coverage of the data and the likelihood that the candidate phase may not completely represent the anisotropy experienced by rays leaving the source region. We performed boot-

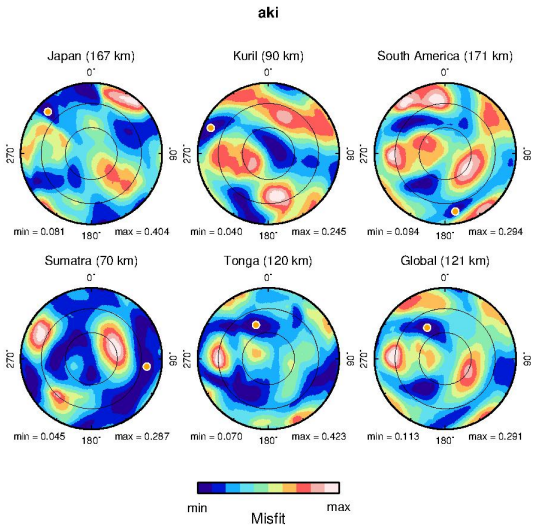

Figure 12. Misfit surfaces for akimotoite. Features as for Figure 9.

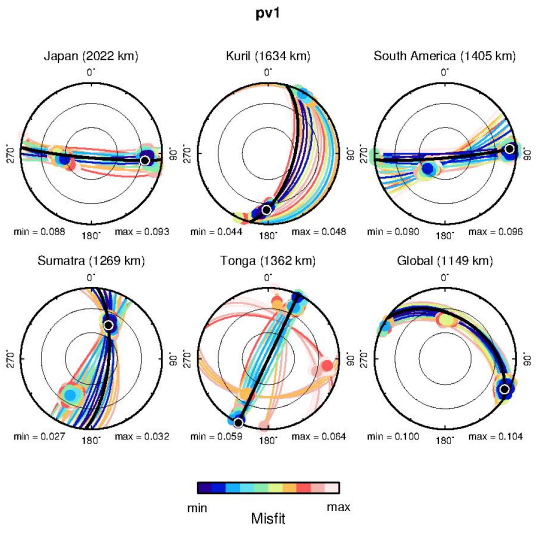

Figure 13. Best-fitting 0.1 % of shear planes (coloured lines) and directions (circles) for each regions and the global dataset from the inversion for the orientation of the deformed pv with $\gamma = 1$. Black planes and directions show the minimum misfit orientations, with other features as described in Figure 9.

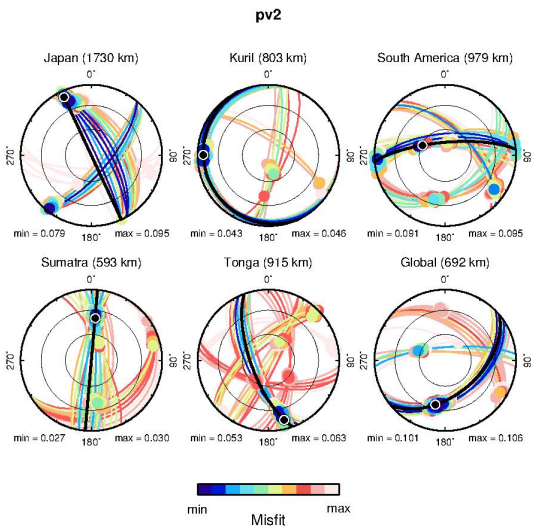

Figure 14. Best-fitting 0.1 % of shear planes (coloured lines) and directions (circles) for each regions and the global dataset from the inversion for the orientation of the deformed pv with $\gamma = 2$. Other features as described in Figure 13.

strap analysis by randomly resampling each dataset with replacement and inverting many times, and the misfit patterns appear robust.

Taking the regions with the greatest coverage (South America, Kuril and Tonga), we note that for the hexagonal elastic constants in the slab frame, each inversion reveals regions of low misfit in common. These are the primary contributors to the Global misfit surface, and suggest that these regions share also a common mechanism which we can interpret. It is also possible that other regions do, but the number of observations is much smaller and hence there are many misfit minima. These directions are near to being within the slab (on the line joining 0° and 180°), and approximately in the subduction direction (near the centre of the the plots). This is consistent with flattening (down-dip compression) in the slab for phases D and akimotoite, and in fact the direction closely matches the P-axes of deep earthquake focal mechanisms. It could also be attributed to some other mechanism causing TTI with the symmetry axis parallel to the dip direction, such as the flattening of pockets of heterogeneous material, but we note that the minimum misfit per observation for TTI is larger (0.12) than for phase D (0.10).

We note that the best-fitting orientation of the TTI, akimotoite and phase D models help explain the observation that δt is not apparently related to path length in the slab. Noting from Figure 8 that in fact few raypaths are within the slab in any case, these mechanisms show the maximum splitting in a girdle around the down-dip direction, and a small amount for rays travelling down along the slab. This effect may cancel out any amplification of the splitting signal from rays which travel a greater distance within the slab.

The best-fitting layer thicknesses for each phase vary between regions and for the global stack. This is partly reflective of the uncertainty in the amount of splitting and tradeoffs between layer thickness and orientation. For TTI, there is clearly a direct trade-off between the TI parameters and the layer thickness, hence in this case the orientation is more informative. For phase D and akimotoite, however, the thicknesses give a fair reflection of the amount of material required to generate the shear wave splitting we see—namely, about 100 km or more. Because there are no data for akimotoite LPO, we have simply imposed rotational symmetry, hence its texture may be artificially strong, potentially explaining the discrepancy between it and phase D.

For the pv constants, there is little consistency between regions. Notably, in order to reproduce the amount of splitting, a layer of at least 1000 km is usually needed. Previous modelling [e.g., *Nippress et al.*, 2004] does not indicate the such strong texturing is likely to be accrued over such a large region. Mostly, best-fitting shear directions are horizontal, but shear planes are usually steeply inclined to the subduction direction, implying slab-oblique shear.

In all cases, we have assumed that the anisotropic layer is made up entirely of the candidate material, and have not taken account of the relative proportion of the phase which is likely to exist in the subducted slab or ambient mantle, to avoid introducing further uncertainties in our inversions. One can approximately infer the true thickness required, assuming the crystals of the other phases in the assemblage are randomly oriented, by multiplying the thicknesses by the inverse of the proportion of the assemblage which is the candidate phase. This would increase the layer thickness required. For pv in the ULM, a value of ∼70 % [*Irifune and Tsuchiya*, 2007] would lead to thicknesses greater by ∼40 %. For akimotoite and phase D, it is highly uncertain what proportion to expect and might vary strongly between slabs; but taking a range of 20 to 50 % would increase the thicknesses by a factor of 2 to 5. At the same time, given current uncertainties in deformation mechanisms in these phases, this effect might be countered by texturing which is stronger than found so far experimentally. Nonetheless, the large volumes of anisotropic material required to fit the observations are a challenge to interpret, and it may be that a combination of effects—such as both LPO and fracture alignment [e.g., *Faccenda*, 2008; *Faccenda et al.*, 2009]—is required.

We also considered inversions in the geographic frame, where the dip of the slab is not considered and results are left relative to the Earth radial direction. The inversion results in this case are not as consistent as when using the slab frame and hence we do not consider them further. For completeness, however, we include them in the Supporting Information (Figures S1–S5).

Lower-hemisphere diagrams showing the P wave velocity and shear wave splitting for the best fitting orientations for each phase are shown in Figure S6.

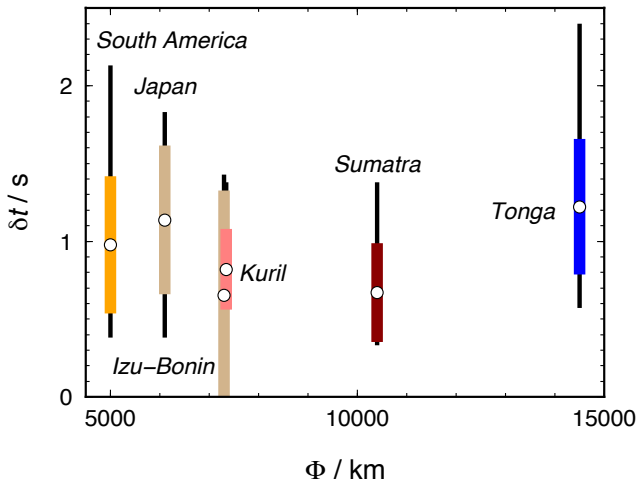

Figure 15. Thermal parameter, Φ, against the range of δt for each deep subduction region. Circles show mean values, coloured bars indicate one standard deviation, whilst the extreme values are shown by the thin black bars.

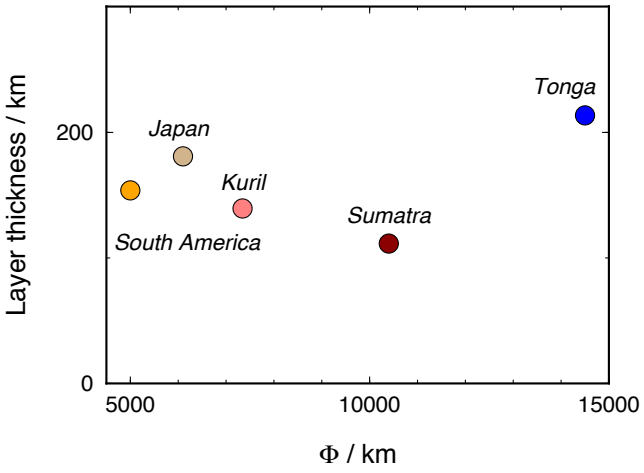

Figure 16. The layer thickness of an olivine aggregate required to best fit shear wave splitting observations for the deepest slab regions, against the thermal parameter, Φ.

4.4. Slab thermal parameter

In order to consider the relationship between the strength of anisotropy and the thermal state of the slab, we compare the amount of splitting or strength of anisotropy to the thermal parameter $\Phi = V\,a \sin\theta$, where V is the converging plate velocity between the overriding and subducting plates, a is the age of the slab, and θ is the dip of the slab [*Kirby et al.*, 1996]. The value of Φ relates to the temperature of the slab at a fixed depth; larger values imply a colder centre of the slab. We take the values for Φ for the deepest regions (Izu-Bonin, Kuril, Japan, South America and Tonga) from *Devaux et al.* [1997] and compare them with δt in Figure 15. If there were a thermally-controlled reason for the anisotropy we observe, then we would expect a variation of δt with Φ if the style of anisotropy is simple. If the events we use occur above or within a metastable olivine wedge, then our observations will be sensitive to this. In this case, calculations suggest that there should be significantly less olivine in the slabs with the smallest Φ (South America, ∼5,000) compared to the largest (Tonga, ∼15,000) [e.g., *Kirby et al.*, 1996]. There is no significant trend in our observations.

If the style of anisotropy is more complicated, however, then a direct comparison with δt may not be applicable, because of the strong directional dependence in shear wave splitting. In this case, we should instead compare Φ with the layer thickness required to fit the observations in the inversions above. We find no correlation, positive or negative, between the inverted layer thickness and Φ for any of our tested mechanisms. Hence we can rule out a thermally-controlled mechanism to the anisotropy in the TZ we observe for the cases we test.

We wish to further test the metastable olivine hypothesis, to formally rule this case out. We perform the same inversions as described above, but for a case representing metastable olivine. We use the average subduction zone constants from *Ismail and Mainprice* [1998], which are taken from natural samples. Although these constants are for uppermost mantle conditions, in our inversions we are insensitive to absolute velocities, so this itself will not affect the results. The anisotropy of olivine does change with pressure and temperature, however, and hence we do not take this in to account—however there are no elasticity data for olivine when metastable, nor natural samples of textured olivine-rich rocks at these conditions, so we believe it is an acceptable compromise.

We show the comparison between Φ and inverted layer thickness for the metastable olivine case in Figure 16. There is no significant positive correlation between the two, and hence with these data we can also rule out this case.

4.5. The cause of deep earthquakes

Significant debate has centred around the underlying cause of earthquakes in the transition zone for many years, with suggestions chiefly focussing on the possibility of metastable olivine [*Kirby et al.*, 1996], as well as melting [*Griggs and Handin*, 1960], dehydration of hydrous phases in fault zones [*Meade and Jeanloz*, 1991] and inherent weakness in hydrous phases [*Raleigh and Paterson*, 1965]. (Mechanisms are reviewed by *Kirby et al.* [1996]). If our observations of seismic anisotropy in the slab region can be ascribed to material within the slab itself, then this potentially sheds light onto the mechanism of deep seismicity.

Because we find no evidence that there is a change in the amount of anisotropy within or beneath the slab with depth, our results do not support the idea that reactions in metastable olivine may not be the cause of earthquakes. However, this assumes that metastable olivine rocks in slabs retain texture; it is possible that olivine is present, but simply does not contribute to seismic anisotropy. On the basis of recent studies suggesting that if olivine is metastable at all in the TZ, it must be dry [*Du Frane et al.*, 2013], and in any case very little should exist [*Mosenfelder et al.*, 2001], we believe that our observations could not of themselves be used to support metastable olivine as a mechanism and perhaps suggest other causes. Conversely, our results do not rule out the decomposition of hydrous phases as causative of deep earthquakes [e.g., *Green and Houston*, 1995; *Meade and Jeanloz*, 1991].

5. Conclusions

We used the method of source-side shear wave splitting to investigate the anisotropy present in the region of deep earthquakes (>200 km) below subduction zones worldwide. A new database of 130 observations was constructed, showing that the transition zone is anisotropic in the region of slabs, and that the strength of the anisotropy does not change with depth or the slab's thermal parameter. On this basis, we conclude that a thermally-controlled process is not responsible for the anisotropy to which our observations are sensitive. Example of this include the presence of metastable olivine or akimotoite.

We inverted the observations for several possible mechanisms causing the anisotropy. For bridgmanite ($MgSiO_3$-perovskite), ∼1,500 km of highly sheared mantle must exist to match the observations, and on this basis we consider perovskite an unlikely cause. For hexagonal, hydrous mineral phases we find that they must be oriented with their rotational symmetry axes pointing up the slab, parallel to the compression directions observed using earthquake focal mechanisms, as predicted from deformation experiments. This suggests that deformation of slab material containing sufficient water to stabilise phases such as D and H is a possible cause of anisotropy within and beneath slabs in the transition zone. These conclusions are subject to the caveats that current knowledge of the deformation mechanisms of TZ materials is poorly known, as are their single-crystal elastic constants, and that we assume a very simple, homogeneous style of deformation. We also cannot rule out the alignment of seismically-distinct material in sub-wavelength pockets, such as might have been created in bending-induced faults in the slab. In either case, our results suggest the possibility that significant volumes of water may be transported at least as far at 660 km into the Earth's mantle.

Appendix A: Shear wave splitting misfit

Here we describe an empirical, objective measure of the misfit between two shear wave splitting operators $\Gamma_i = (\phi_i, \delta t_i)$, $i = 1, 2$. Note that the inverse operator is defined as $\Gamma_i^{-1} = (\phi_i, -\delta t_i)$.

When constructing a measure of misfit, it is desirable to account for the uncertainty in shear wave splitting measurements which are near the null orientations, and to include the characteristic shape of the λ_2 surfaces in $(\phi, \delta t)$ space [e.g., *Silver and Chan*, 1991]. For instance, when the source polarisation of an incoming wave is close to the fast orientation of the medium in that direction, there is typically a much larger uncertainty in δt than in ϕ. Conversely, splitting measurements when the difference between the source polarisation and fast direction is closer to 45° exhibit larger errors in ϕ. A misfit function termed the 'λ_2S splitting misfit' which meets these criteria can be described as follows:

1. Create a synthetic wavelet with dominant frequency and source polarisation the same as that of the data considered. (A Ricker wavelet is suitable for this purpose, however tests indicate that the specific waveform has almost no effect on the final misfit.) This should consist of two orthogonal 'horizontal' traces.

2. Apply the first shear wave splitting operator, Γ_1, to the wavelet.

3. Apply the inverse of the second operator, Γ_2^{-1}, to the wavelet.

4. Compute the covariance matrix of the split horizontal traces.

5. Find the two eigenvalues of the covariance matrix, $\lambda_1 \geq \lambda_2$.

6. The misfit is given by λ_1/λ_2.

In order to remove the ambiguity of which operator to term the first, and which the second, we perform the calculation of the misfit for both orders (Γ_1, Γ_2^{-1} and Γ_2, Γ_1^{-1}), then compute the arithmetic mean of the two misfits to give the final misfit.

Acknowledgments. We thank two anonymous reviewers and Manuele Faccenda for constructive comments which helped improve the manuscript. The data for this paper are available from the Data Management Center (DMC) of the Incorporated Research Institutions for Seismology (IRIS; http://iris.edu/), using the information in Supporting Information Table S1. Some data were gathered by the Afar Rift Consortium. We thank A. Rosa for the phase D ODFs, and D. Mainprice for those of pv. The research leading to these results has received funding from the European Research Council under the European Union's Seventh Framework Programme (FP7/2007–2013)/ERC Grant agreement 240473 "CoMITAC". Asher Pemberton was supported by a NERC Research Experience Placement. Computation was performed using the CoMITAC cluster 'Typhon'.

References

Akaogi, M., A. Tanaka, and E. Ito (2002), Garnet—ilmenite—perovskite transitions in the system $Mg_4Si_4O_{12}$—$Mg_3Al_2Si_3O_{12}$ at high pressures and high temperatures: phase equilibria, calorimetry and implications for mantle structure, *Phys. Earth Planet. Inter.*, *132*, 303–324, doi:10.1016/S0031-9201(02)00075-4.

Ayele, A., G. Stuart, and J.-M. Kendall (2004), Insights into rifting from shear wave splitting and receiver functions: an example from Ethiopia, *Geophys J Int*, *157*, 354–362, doi:10.1111/j.1365-246X.2004.02206.x.

Barruol, G., and R. Hoffmann (1999), Upper mantle anisotropy beneath the Geoscope stations, *J Geophys Res-Sol Ea*, *104*, 10,757–10,773.

Barruol, G., G. Helffrich, and A. Vauchez (1997), Shear wave splitting around the northern Atlantic: frozen Pangaean lithospheric anisotropy?, *Tectonophysics*, *279*, 135–148, doi:10.1016/S0040-1951(97)00126-1.

Chen, W.-P., and M. R. Brudzinksi (2003), Seismic anisotropy in the mantle transition zone beneath Fiji-Tonga, *Geophys Res Lett*, *30*, 1682, doi:10.1029/2002GL016330.

Cordier, P., T. Ungar, L. Zsoldos, and G. Tichy (2004), Dislocation creep in $MgSiO_3$ perovskite at conditions of the Earth's uppermost lower mantle, *Nature*, *428*, 837–840, doi:10.1038/nature02472.

DeMets, C., R. G. Gordon, D. F. Argus, and S. Stein (1994), Effect of recent revisions to the geomagnetic reversal time scale on estimates of current plate motions, *Geophys Res Lett*, *21*, 2191–2194, doi:10.1029/94GL02118.

Devaux, J. P., G. Schubert, and C. Anderson (1997), Formation of a metastable olivine wedge in a descending slab, *J Geophys Res-Sol Ea*, *102*, 24,627–24,673, doi:10.1029/97JB02334.

Di Leo, J. F., J. Wookey, J. O. S. Hammond, J.-M. Kendall, S. Kaneshima, H. Inoue, T. Yamashina, and P. Parjadi (2012), Mantle flow in regions of complex tectonics: Insights from Indonesia, *Geochemistry Geophysics Geosystems*, *13*, Q12,008, doi:10.1029/2012GC004417.

Du Frane, W. L., T. G. Sharp, J. L. Mosenfelder, and K. Leinenweber (2013), Ringwoodite growth rates from olivine with similar to 75 ppmw H_2O: Metastable olivine must be nearly anhydrous to exist in the mantle transition zone, *Phys. Earth Planet. Inter.*, *219*, 1–10, doi:10.1016/j.pepi.2013.04.001.

Faccenda, M. (2014), Water in the slab: A trilogy, *Tectonophysics*, *614*, 1–30, doi:10.1016/j.tecto.2013.12.020.

Faccenda, M., T. V. Gerya, and L. Burlini (2009), Deep slab hydration induced by bending-related variations in tectonic pressure, *Nature Geosci*, *2*(11), 790–793, doi:10.1038/ngeo656.

Faccenda, M. a. (2008), Fault-induced seismic anisotropy by hydration in subducting oceanic plates, *Nature*, *455*, 1097–1100, doi:10.1038/nature07376.

Foley, B. J., and M. Long (2011), Upper and mid-mantle anisotropy beneath the Tonga slab, *Geophys Res Lett*, *38*, L02,303, doi:10.1029/2010GL046021.

Fouch, M. J., and K. M. Fischer (1996), Mantle anisotropy beneath northwest Pacific subduction zones, *J. Geophys. Res.*, *101*, 15,987–16,002.

Fouch, M. J., K. M. Fischer, E. Parmentier, M. Wysession, and T. Clarke (2000), Shear wave splitting, continental keels, and patterns of mantle flow, *J Geophys Res-Sol Ea*, *105*, 6255–6275, doi:10.1029/1999JB900372.

Green, H. W., and H. Houston (1995), The mechanics of deep earthquakes, *Annu Rev Earth Planet Sci*, *23*, 169–213, doi:10.1146/annurev.ea.23.050195.001125.

Griggs, D., and J. Handin (1960), Observations on fracture and a hypothesis of earthquakes, in *Rock Deformation*, vol. 79, edited by D. Griggs and J. Handin, pp. 347–364, Geological Society of America Memoirs, doi:10.1130/MEM79-p347.

Hall, S. A., J.-M. Kendall, and M. V. der Baan (2004), Some comments on the effects of lower-mantle anisotropy on SKS and SKKS phases, *Phys. Earth Planet. Inter.*, *146*, 469–481, doi:10.1016/j.pepi.2004.05.002.

Hayes, G. P., D. J. Wald, and R. L. Johnson (2012), Slab1.0: A three-dimensional model of global subduction zone geometries, *J. Geophys. Res.*, *117*, B01,302, doi:10.1029/2011JB008524.

Higo, Y., T. Inoue, B. Li, T. Irifune, and R. Liebermann (2006), The effect of iron on the elastic properties of ringwoodite at high pressure, *Phys. Earth Planet. Inter.*, *159*, 276–285, doi:10.1016/j.pepi.2006.08.004.

Hirschmann, M. M. (2006), Water, melting and the deep Earth H_2O cycle, *Annu Rev Earth Planet Sci*, *34*, 629–653, doi:10.1146/annurev.earth.34.031405.125211.

Irifune, T., and T. Tsuchiya (2007), Mineralogy of the Earth—Phase transitions and mineralogy of the lower mantle, in *Treatise on Geophysics*, vol. 2, Mineral Physics, edited by G. Price and G. Schubert, pp. 33–62, Elsevier Science.

Ismail, W. B., and D. Mainprice (1998), An olivine fabric database: an overview of upper mantle fabrics and seismic anisotropy, *Tectonophysics*, *296*, 145–157, doi:10.1016/S0040-1951(98)00141-3.

Kárason, H., and R. van der Hilst (2000), Constraints on mantle convection from seismic tomography, in *The History and Dynamics of Global Plate Motions*, edited by M. A. Richards, R. G. Gordon, and R. van der Hilst, pp. 277–288, American Geophysical Union Geophysical Monograph 121, Washington, D.C., USA, doi:10.1029/GM121.

Kavner, A. (2003), Elasticity and strength of hydrous ringwoodite at high pressure, *Earth Planet Sci Lett*, *214*, 645–654, doi:10.1016/S0012-821X(03)00402-3.

Kendall, J.-M., and C. J. Thomson (1993), Seismic modelling of subduction zones with inhomogeneity and anisotropy–i. Teleseismic P-wave-front tracking, *Geophys. J. Int.*, *112*, 39–66, doi:10.1111/j.1365-246X.1993.tb01435.x.

Kennett, B., E. Engdahl, and R. Buland (1995), Constraints on seismic velocities in the Earth from travel-times, *Geophys J Int*, *122*, 108–124, doi:10.1111/j.1365-246X.1995.tb03540.x.

Kirby, S., S. Stein, E. Okal, and D. Rubie (1996), Metastable mantle phase transformations and deep earthquakes in subducting oceanic lithosphere, *Reviews of Geophysics*, *34*, 261–306.

Kustowski, B., G. Ekström, and A. Dziewoński (2008), Anisotropic shear-wave velocity structure of the Earth's mantle: A global model, *J Geophys Res-Sol Ea*, *113*, B06,306, doi:10.1029/2007JB005169.

Li, L., D. Weidner, J. P. Brodholt, D. Alfè, and G. Price (2006), Elasticity of Mg_2SiO_4 ringwoodite at mantle conditions, *Phys. Earth Planet. Inter.*, *157*, 181–187, doi:10.1016/j.pepi.2006.04.002.

Li, L., D. Weidner, J. P. Brodholt, D. Alfè, and G. Price (2009), Ab initio molecular dynamics study of elasticity of akimotoite $MgSiO_3$ at mantle conditions, *Phys. Earth Planet. Inter.*, *173*, 115–120, doi:10.1016/j.pepi.2008.11.005.

Liu, K. H. (2009), NA-SWS-1.1: A uniform database of teleseismic shear wave splitting measurements for North America, *Geochem Geophy Geosy*, *10*, Q05,011, doi:10.1029/2009GC002440.

Liu, L. (1987), Effects of H_2O on the phase behaviour of the forsterite-enstatite system at high pressures and temperatures and implications for the Earth, *Phys. Earth Planet. Inter.*, *49*, 142–167, doi:10.1016/0031-9201(87)90138-5.

Liu, L.-G. (1976), The high-pressure phases of $MgSiO_3$, *Earth Planet Sci Lett*, *31*, 200–208, doi:10.1016/0012-821X(76)90212-0.

Lynner, C., and M. D. Long (2014), Testing models of sub-slab anisotropy using a global compilation of source-side shear wave splitting data, *J Geophys Res-Sol Ea*, *119*, 7226–7244, doi:10.1002/2014JB010983.

Mainprice, D. (2007), Seismic anisotropy of the deep earth from a mineral and rock physics perspective, in *Treatise on Geophysics*, vol. 2, Mineral Physics, edited by G. Price and G. Schubert, pp. 437–492, Elsevier Science.

Mainprice, D., A. Tommasi, D. Ferré, P. Carrez, and P. Cordier (2008), Predicted glide systems and crystal preferred orientations of polycrystalline silicate Mg-perovskite at high pressure: Implications for the seismic anisotropy in the lower mantle, *Earth Planet Sci Lett*, *271*, 135–144, doi:10.1016/j.epsl.2008.03.058.

Masson, D. (1991), Fault patterns at outer trench walls, *Marine Geophysical Researches*, *13*, 209–225, doi:10.1007/BF00369150.

Meade, C., and R. Jeanloz (1991), Deep-focus earthquakes and recycling of of water into the Earth's mantle, *Science*, *252*, 68–72.

Montagner, J.-P., and B. Kennett (1996), How to reconcile body-wave and normal-mode reference earth models, *Geophys J Int*, *125*, 229–248, doi:10.1111/j.1365-246X.1996.tb06548.x.

Montelli, R., G. Nolet, F. Dahlen, G. Masters, E. Engdahl, and S. Hung (2004), Finite-frequency tomography reveals a variety of plumes in the mantle, *Science*, *303*, 338–343, doi:10.1126/science.1092485.

Mosenfelder, J. L., F. C. Marton, C. R. I. Ross, L. Kerschhofer, and D. C. Rubie (2001), Experimental constraints on the depth of olivine metastability in subducting lithosphere, *Phys. Earth Planet. Inter.*, *127*, 165–180, doi:10.1016/S0031-9201(01)00226-6.

Murakami, M., S. Sinogeikin, K. Litasov, E. Ohtani, and J. D. Bass (2008), Single-crystal elasticity of iron-bearing majorite to 26 GPa: Implications for seismic velocity structure of the mantle transition zone, *Earth Planet Sci Lett*, *274*, 339–345, doi:10.1016/j.epsl.2008.07.045.

Nippress, S. E. J., N. Kusznir, and J.-M. Kendall (2004), Modeling of lower mantle seismic anisotropy beneath subduction zones, *Geophys Res Lett*, *31*, L19,612, doi:10.1029/2004GL020701.

Nishi, M., T. Irifune, J. Tsuchiya, Y. Tange, Y. Nishihara, K. Fujino, and Y. Higo (2014), Stability of hydrous silicate at high pressures and water transport to the deep lower mantle, *Nature Geosci*, pp. 1–11, doi:10.1038/ngeo2074.

Niu, F., and A. Perez (2004), Seismic anisotropy in the lower mantle: A comparison of waveform splitting of SKS and SKKS, *Geophys Res Lett*, *31*, L24,612, doi:10.1029/2004GL021196.

Nowacki, A., J. Wookey, and J.-M. Kendall (2010), Deformation of the lowermost mantle from seismic anisotropy, *Nature*, *467*, 1091–1095, doi:10.1038/nature09507.

Nowacki, A., J. Wookey, and J.-M. Kendall (2011), New advances in using seismic anisotropy, mineral physics and geodynamics to understand deformation in the lowermost mantle, *Journal of Geodynamics*, *52*, 205–228, doi:10.1016/j.jog.2011.04.003.

Nowacki, A., J.-M. Kendall, and J. Wookey (2012), Mantle anisotropy beneath the Earth's mid-ocean ridges, *Earth Planet Sci Lett*, *317-318*, 56–67, doi:10.1016/j.epsl.2011.11.044.

Ohtani, E. (2005), Water in the mantle, *Elements*, *1*, 25–30.

Ohuchi, T., K. Fujino, T. Kawazoe, and T. Irifune (2014), Crystallographic preferred orientation of wadsleyite and ringwoodite: Effects of phase transformation and water on seismic anisotropy in the mantle transition zone, *Earth Planet Sci Lett*, *397*, 133–144, doi:10.1016/j.epsl.2014.03.066.

Panning, M., and B. Romanowicz (2004), Inferences on flow at the base of Earth's mantle based on seismic anisotropy, *Science*, *303*, 351–353, doi:10.1126/science.1091524.

Panning, M., and B. Romanowicz (2006), A three-dimensional radially anisotropic model of shear velocity in the whole mantle, *Geophys J Int*, *167*, 361–379, doi:10.1111/j.1365-246X.2006.03100.x.

Raleigh, C., and M. Paterson (1965), Experimental deformation of serpentine and its tectonic implications, *J Geophys Res*, *70*, 3965–3985.

Ranero, C., and V. Sallarès (2004), Geophysical evidence for hydration of the crust and mantle of the nazca plate during bending at the north chile trench, *Geol*, *32*, 549, doi:10.1130/G20379.1.

Restivo, A., and G. Helffrich (2006), Core-mantle boundary structure investigated using SKS and SKKS polarization anomalies, *Geophys J Int*, *165*, 288–302, doi:10.1111/j.1365-246X.2006.02901.x.

Rosa, A. D., C. Sanchez-Valle, and S. Ghosh (2012), Elasticity of phase D and implication for the degree of hydration of deep subducted slabs, *Geophys Res Lett*, *39*, L06,304, doi:10.1029/2012GL050927.

Rosa, A. D., C. Sanchez-Valle, C. Nisr, S. R. Evans, R. Debord, and S. Merkel (2013), Shear wave anisotropy in textured phase D and constraints on deep water recycling in subduction zones, *Earth Planet Sci Lett*, *377-378*, 13–22, doi:10.1016/j.epsl.2013.06.036.

Shiraishi, R., E. Ohtani, K. Kanagawa, A. Shimojuku, and D. Zhao (2008), Crystallographic preferred orientation of akimotoite and seismic anisotropy of tonga slab, *Nature*, *455*, 657–660, doi:10.1038/nature07301.

Silver, P. G., and W. W. Chan (1991), Shear-wave splitting and subcontinental mantle deformation, *J Geophys Res-Sol Ea*, *96*, 16,429–16,454, doi:10.1029/91JB00899.

Smith, W. H. F., and P. Wessel (1990), Gridding with continuous curvature splines in tension, *Geophysics*, *55*, 293–305.

Tandon, G., and G. Weng (1984), The effect of aspect ratio of inclusions on the elastic properties of unidirectionally aligned composites, *Polym Composite*, *5*, 327–333, doi:10.1002/pc.750050413.

Thomsen, L. (1986), Weak elastic anisotropy, *Geophysics*, *51*, 1954–1966, doi:10.1190/1.1442051.

Thurel, E., and P. Cordier (2003), Plastic deformation of wadsleyite: I. high-pressure deformation in compression, *Physics And Chemistry Of Minerals*, *30*, 256–266, doi:10.1007/s00269-003-0312-8.

Thurel, E., P. Cordier, D. J. Frost, and S.-I. Karato (2003), Plastic deformation of wadsleyite: II. high-pressure deformation in shear, *Physics And Chemistry Of Minerals*, *30*, 267–270, doi:10.1007/s00269-003-0313-7.

Tommasi, A. (2004), Strain-induced seismic anisotropy of wadsleyite polycrystals and flow patterns in the mantle transition zone, *Journal Of Geophysical Research*, *109*(B12), B12,405, doi:10.1029/2004JB003158.

Tong, C., O. Gudmundsson, and B. Kennett (1994), Shear wave splitting in refracted waves returned from the upper mantle transition zone beneath northern Australia, *J Geophys Res*, *99*, 15,783–15,797, doi:10.1029/94JB00460.

Trampert, J., and H. J. van Heijst (2002), Global azimuthal anisotropy in the transition zone, *Science*, *296*, 1297–1299, doi:10.1126/science.1070264.

Walker, A. M., and J. Wookey (2012), MSAT—A new toolkit for the analysis of elastic and seismic anisotropy, *Computers & Geosciences*, *49*, 81–90, doi:10.1016/j.cageo.2012.05.031.

Wenk, H.-R., I. Lonardeli, J. Pehl, J. Devine, V. Prakapenka, G. Shen, and H.-K. Mao (2004), In situ observation of texture development in olivine, ringwoodite, magnesiowüstite and silicate perovskite at high pressure, *Earth Planet Sci Lett*, *226*, 507–519, doi:10.1016/j.epsl.2004.07.033.

Wookey, J., and J.-M. Kendall (2004), Evidence of midmantle anisotropy from shear wave splitting and the influence of shear-coupled P waves, *J Geophys Res-Sol Ea*, *109*, B07,309, doi:10.1029/2003JB002871.

Wookey, J., J.-M. Kendall, and G. Barruol (2002), Mid-mantle deformation inferred from seismic anisotropy, *Nature*, *415*, 777–780.

Wookey, J., J.-M. Kendall, and G. Rümpker (2005), Lowermost mantle anisotropy beneath the north Pacific from differential S–ScS splitting, *Geophys J Int*, *161*, 829–838, doi:10.1111/j.1365-246X.2005.02623.x.

Yu, Y. G., R. M. Wentzcovitch, V. L. Vinograd, and R. J. Angel (2011), Thermodynamic properties of $MgSiO_3$ majorite and phase transitions near 660 km depth in $MgSiO_3$ and Mg_2SiO_4: A first principles study, *J Geophys Res-Sol Ea*, *116*, B02,208, doi:10.1029/2010JB007912.

Yuan, K., and C. Beghein (2013), Seismic anisotropy changes across upper mantle phase transitions, *Earth Planet Sci Lett*, doi:10.1016/j.epsl.2013.05.031.

Zha, C., T. Duffy, H.-K. Mao, R. Downs, R. Hemley, and D. Weidner (1997), Single-crystal elasticity of β-Mg_2SiO_4 to the pressure of the 410 km seismic discontinuity in the Earth's mantle, *Earth Planet Sci Lett*, *147*, E9–E15, doi:10.1016/S0012-821X(97)00010-1.

Zhang, Y., D. Zhao, and M. Matsui (2005), Anisotropy of akimotoite: A molecular dynamics study, *Phys. Earth Planet. Inter.*, *151*, 309–319, doi:10.1016/j.pepi.2005.04.003.

Corresponding author: A. Nowacki, School of Earth Sciences, University of Bristol, Wills Memorial Building, Queen's Road, Bristol, BS8 1RJ, UK. (andy.nowacki@bristol.ac.uk)

Supporting Information for "Mid-mantle anisotropy in subduction zones and deep water transport"

Andy Nowacki[1], J.-Michael Kendall[1], James Wookey[1] and Asher Pemberton[1]

Contents of this file

1. Text S1 to S2
2. Figures S1 to S6
3. Tables S1 to S2

Additional Supporting Information (Files uploaded separately)

1. Table S2 (`Nowackietal-ts02.txt`)

Introduction

Included in these auxiliary materials is a file containing the raw results of the above study, listing the earthquake time and location, seismometer name and location, analysis windows of the shear wave splitting analysis, and the results of the analysis. We also

---

Corresponding author: A. Nowacki, School of Earth Sciences, University of Bristol, Wills Memorial Building, Queen's Road, Bristol, BS8 1RJ, UK. (andy.nowacki@bristol.ac.uk)

[1]School of Earth Sciences, University of Bristol, Bristol, UK

provide figures showing the geographic-frame fits discussed in the text and details of the receiver-side splitting corrections used.

Text S1. Geographic frame fits

In addition to inverting for the best fitting orientation in the slab frame, we also repeated the process in the geographic frame. In this orientation, we again rotate our results so that the slab strikes at 0°, but do not rotate about the slab strike, meaning our results can be thought of as relative to the Earth's surface. In Figures S1–S5 the Earth's radial direction is through the centre of the lower hemispheres. This procedure should reveal if there are any processes related to radial phenomena (e.g., the viscosity increase at the 660) more clearly than results presented in the slab frame.

We note that pv shear planes are more frequently perpendicular or highly oblique to subduction strike and shear directions are usually strike-parallel, which is not consistent with shearing of the slab across the top of the lower mantle (left to right in these figures). Similarly, orientations of the hexagonal elastic constants are generally such that the axis of symmetry is horizontal, which is again not consistent with horizontal shearing if basal slip is the dominant deformation mechanism.

Text S2. Best-fitting orientations of candidate phases

In this section we show the velocity surfaces for the candidate phases when in the best-fitting orientations, in the slab frame. Because these are lower hemisphere projections, they can be compared with Figure 8 of the main text.

References

Ayele, A., G. Stuart, and J.-M. Kendall (2004), Insights into rifting from shear wave splitting and receiver functions: an example from Ethiopia, *Geophys J Int*, *157*, 354–362, doi:10.1111/j.1365-246X.2004.02206.x.

Barruol, G., and R. Hoffmann (1999), Upper mantle anisotropy beneath the Geoscope stations, *J Geophys Res-Sol Ea*, *104*, 10,757–10,773.

Barruol, G., G. Helffrich, and A. Vauchez (1997), Shear wave splitting around the northern Atlantic: frozen Pangaean lithospheric anisotropy?, *Tectonophysics*, *279*, 135–148, doi: 10.1016/S0040-1951(97)00126-1.

Fouch, M. J., K. M. Fischer, E. Parmentier, M. Wysession, and T. Clarke (2000), Shear wave splitting, continental keels, and patterns of mantle flow, *J Geophys Res-Sol Ea*, *105*, 6255–6275, doi:10.1029/1999JB900372.

Liu, K. H. (2009), NA-SWS-1.1: A uniform database of teleseismic shear wave splitting measurements for North America, *Geochem Geophy Geosy*, *10*, Q05,011, doi: 10.1029/2009GC002440.

Niu, F., and A. Perez (2004), Seismic anisotropy in the lower mantle: A comparison of waveform splitting of SKS and SKKS, *Geophys Res Lett*, *31*, L24,612, doi: 10.1029/2004GL021196.

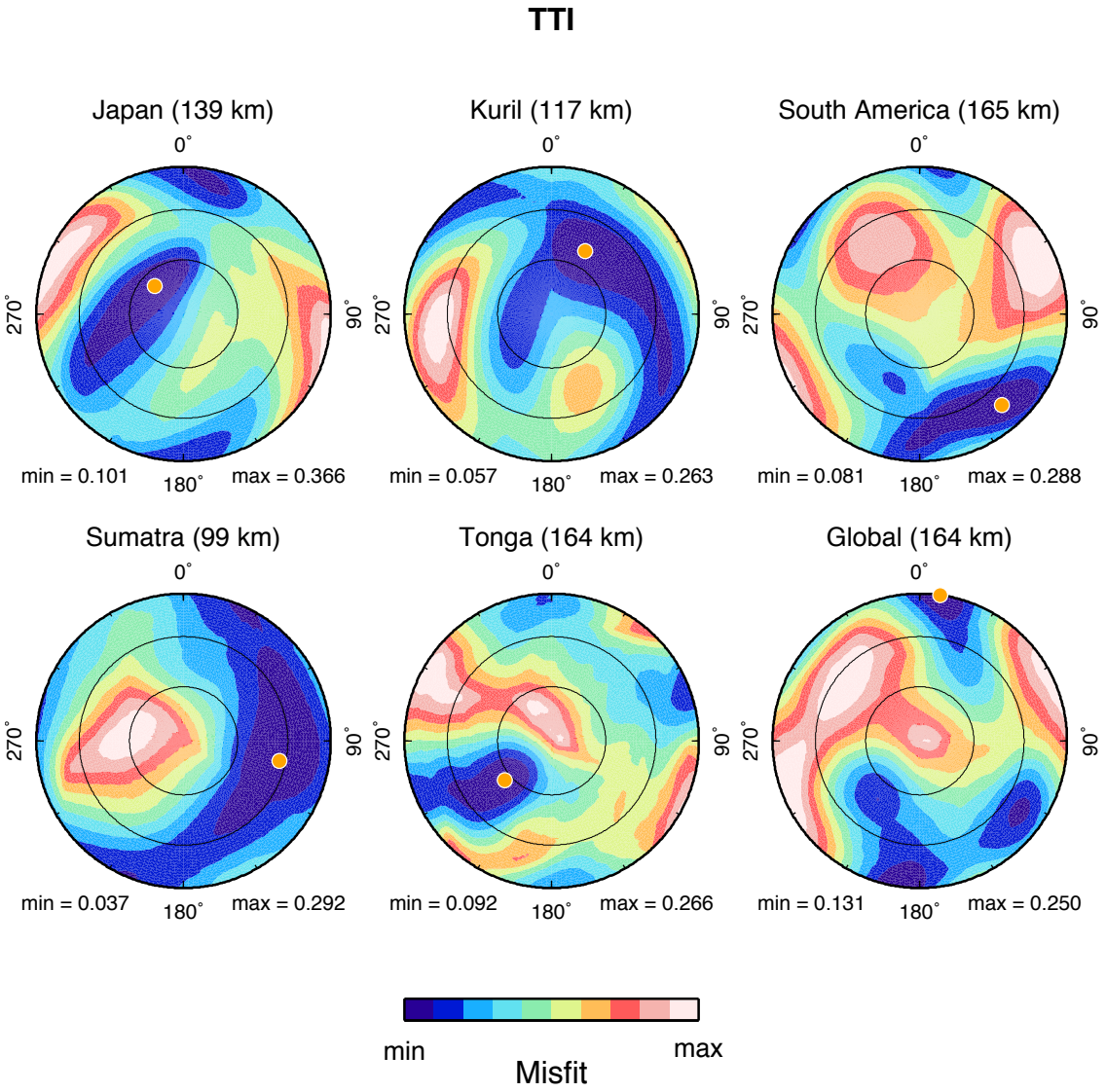

Figure S1. Misfit surfaces for each region and the global dataset from the inversion for the orientation of the rotational symmetry axis of TTI. Lower hemisphere, equal area projections are in the geographic frame (see text), and show the misfit per observation, with black circles spaced at 30° of incidence angle. Colour bar at bottom goes from minimum (blue) to maximum (pink) misfit for each region. Orange circles show the minimum misfit orientation. Distance in brackets above each plot shows the best-fitting layer thickness of the elastic constants.

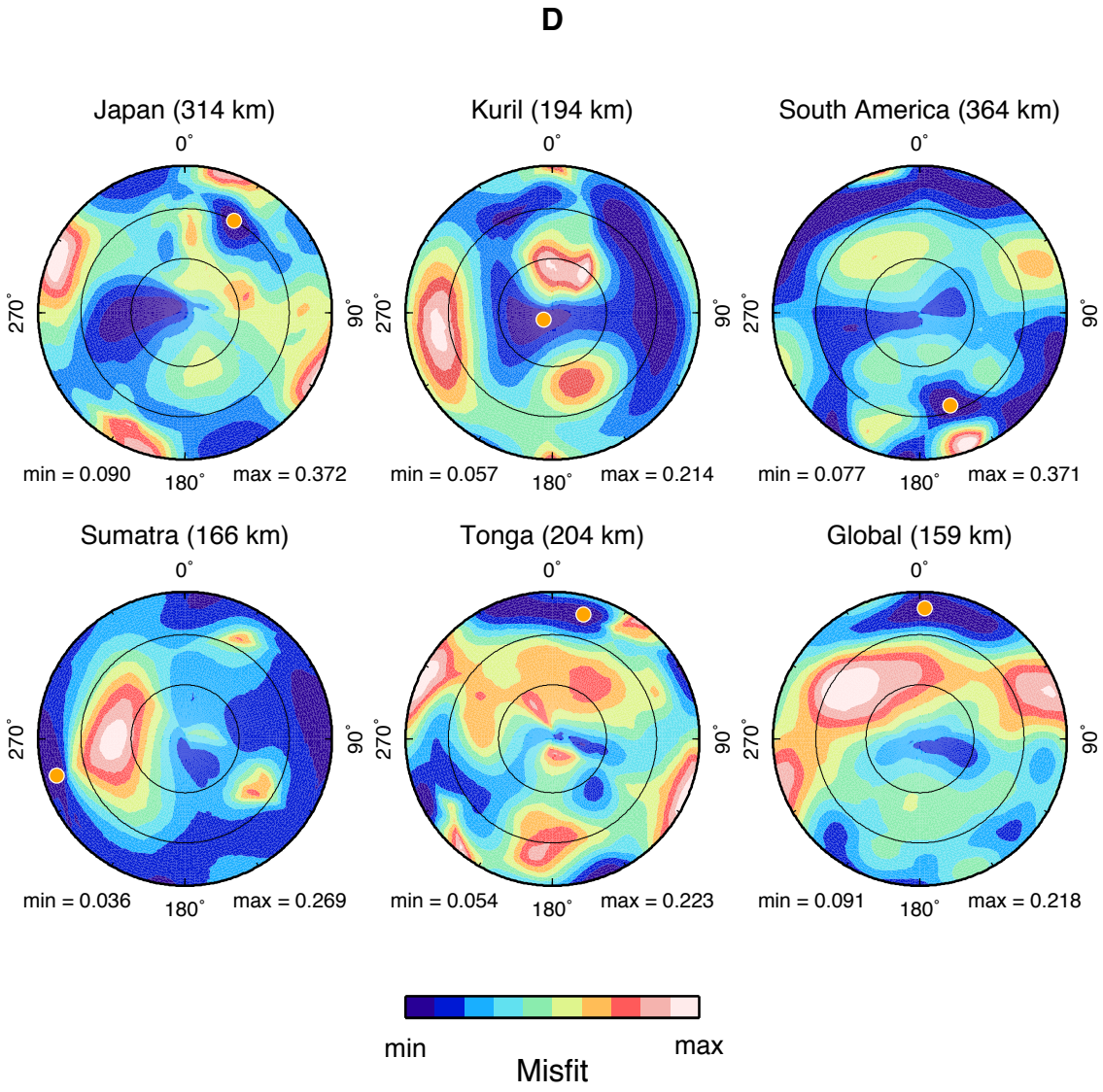

Figure S2. Misfit surfaces for deformed phase D. Features as for Figure S1.

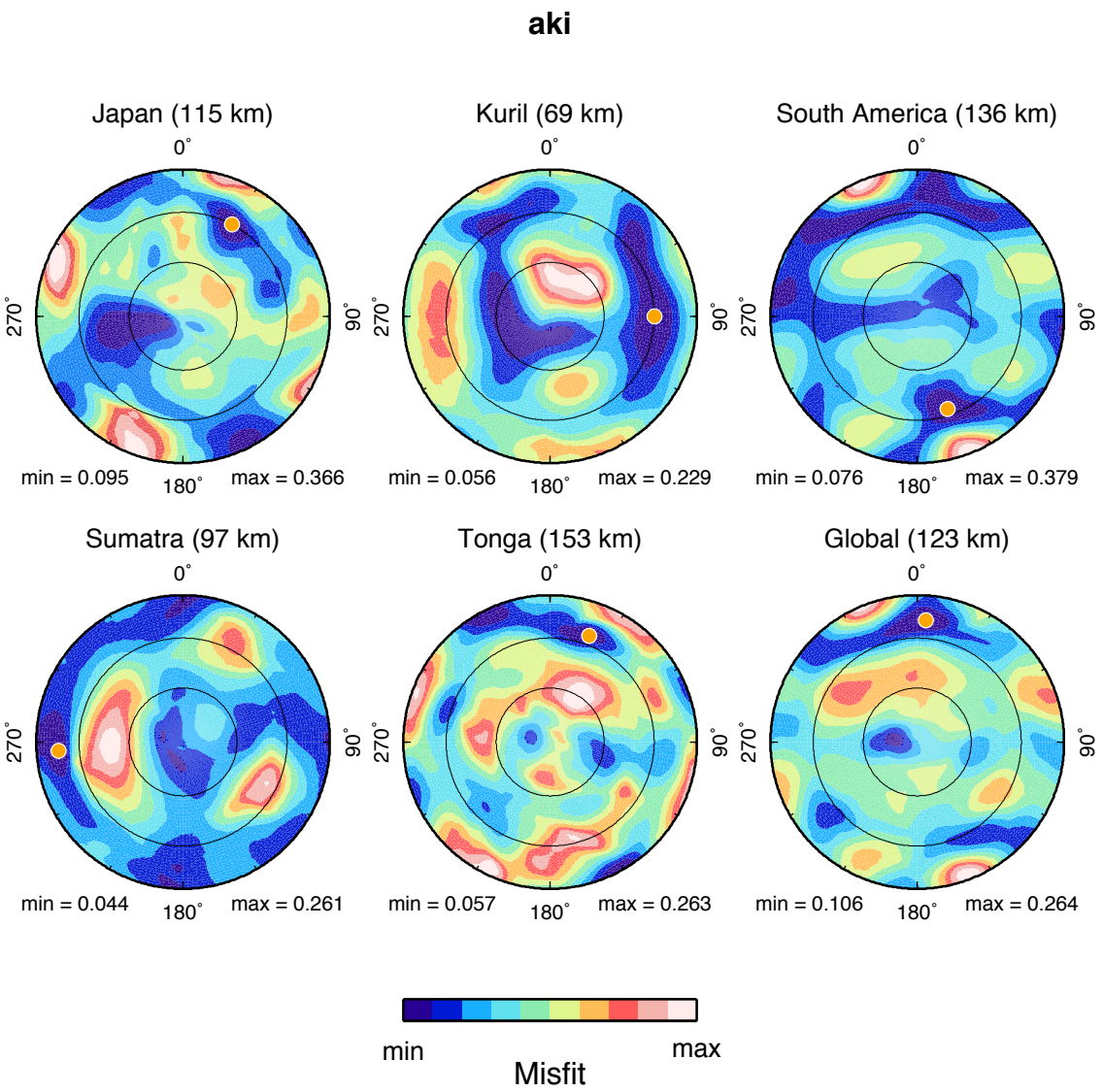

Figure S3. Misfit surfaces for akimotoite. Features as for Figure S1.

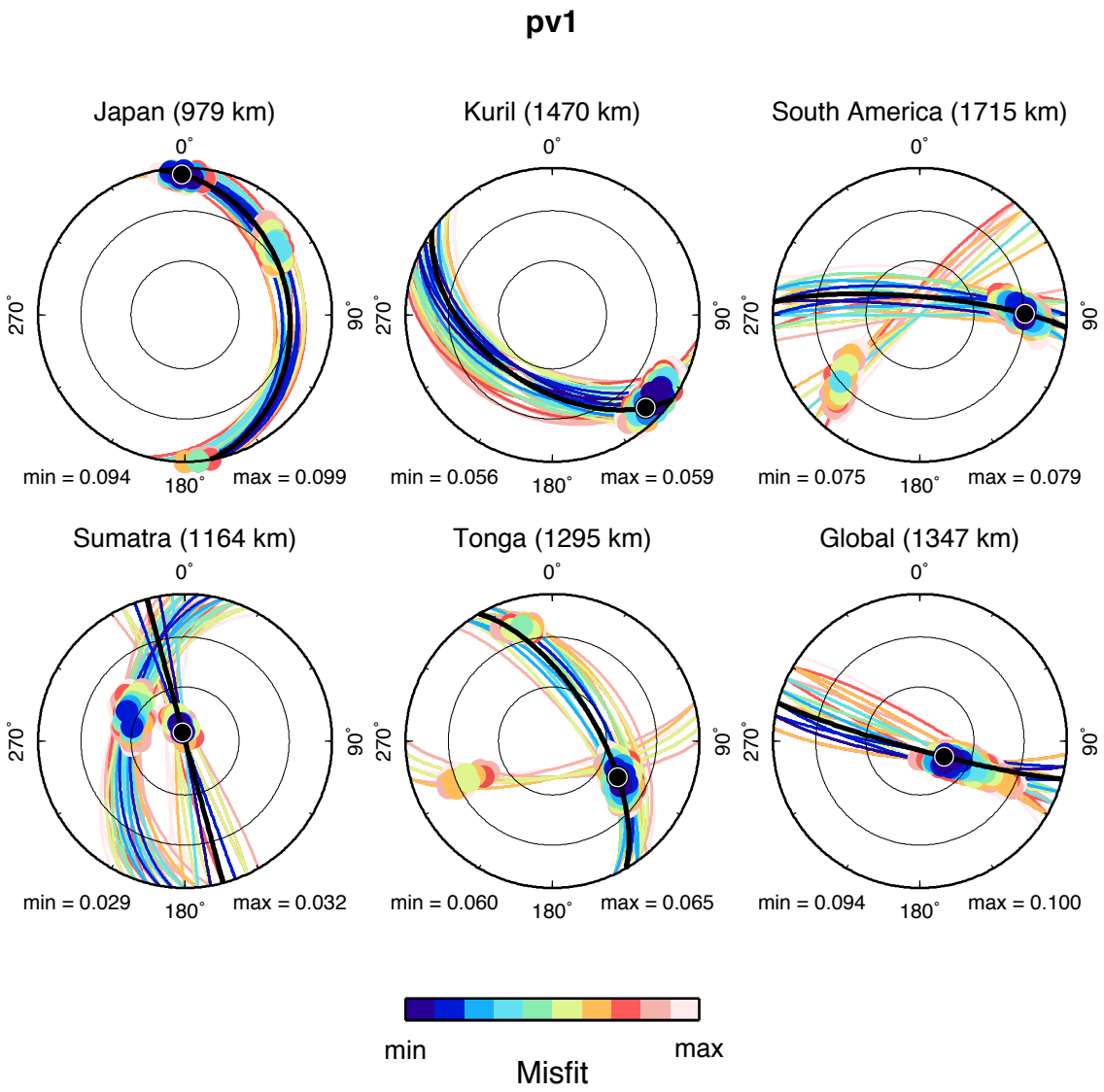

Figure S4. Best-fitting 0.1 % of shear planes (coloured lines) and directions (circles) for each regions and the global dataset from the inversion for the orientation of the deformed pv with $\gamma = 1$. Black planes and directions show the minimum misfit orientations, with other features as described in Figure S1.

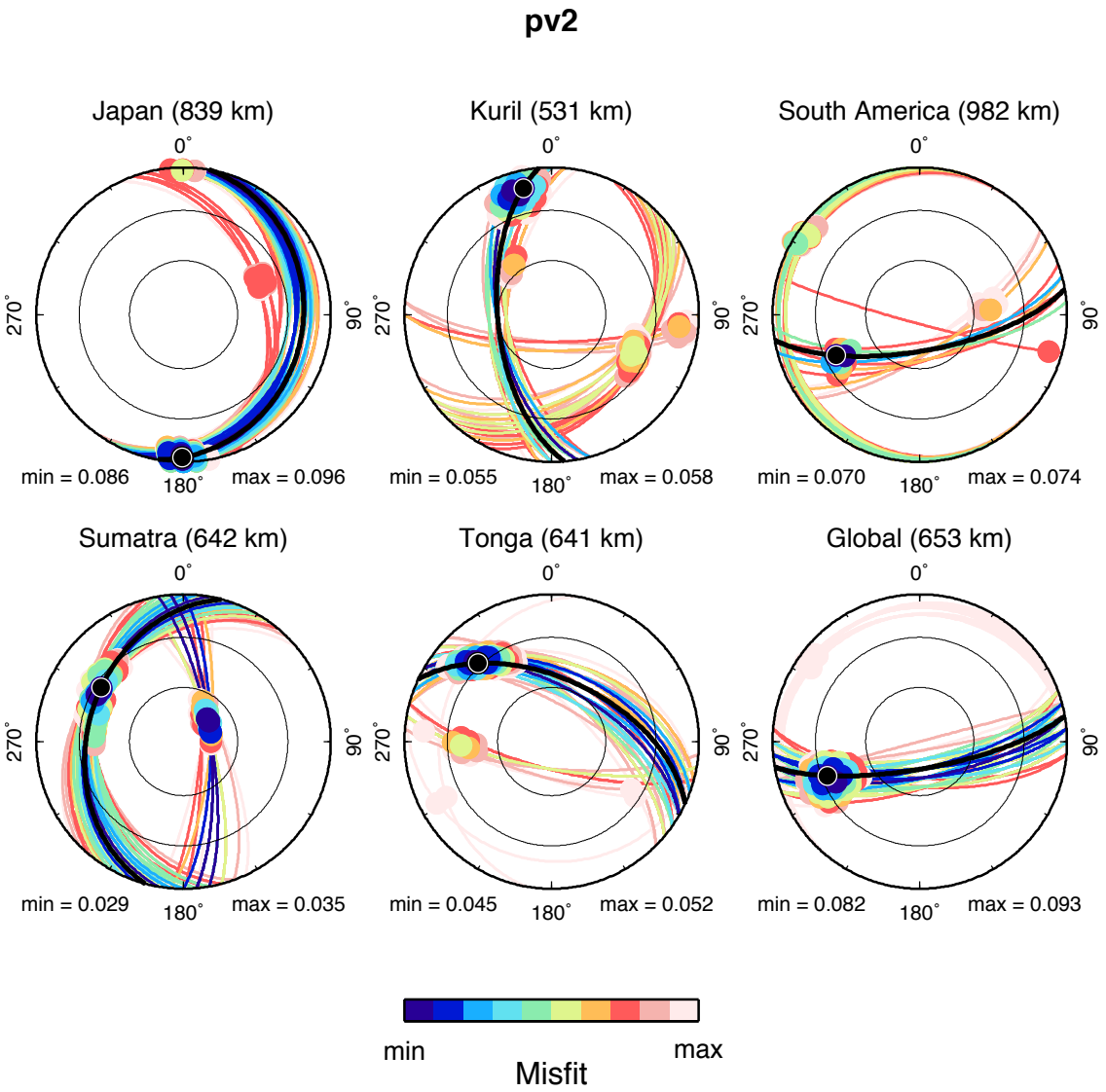

Figure S5. Best-fitting 0.1 % of shear planes (coloured lines) and directions (circles) for each regions and the global dataset from the inversion for the orientation of the deformed pv with $\gamma = 2$. Other features as described in Figure S5.

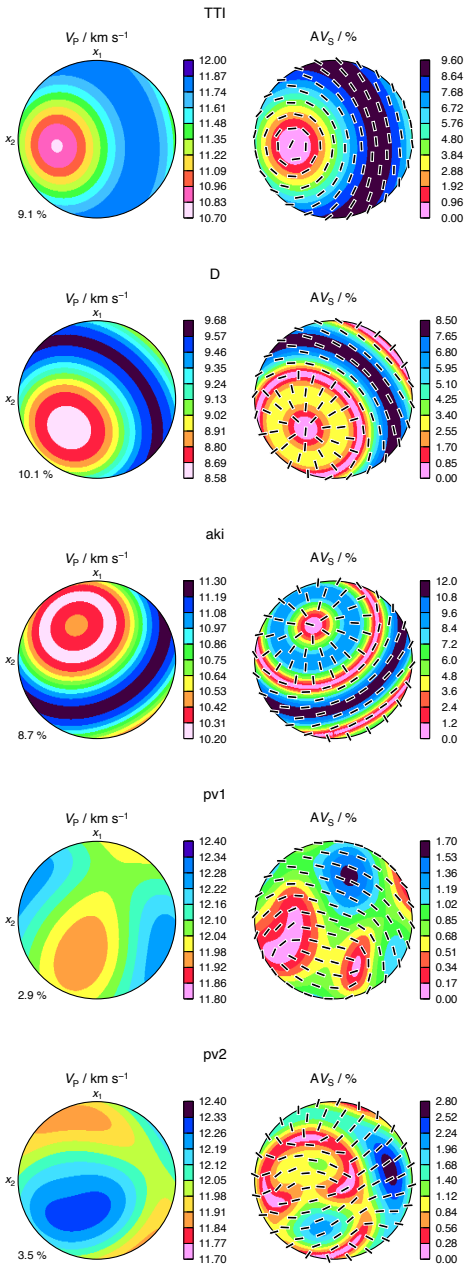

Figure S6. Best fitting orientations of each candidate phase, from top to bottom: TTI, phase D, akimotoite, perovskite ($\gamma = 1$) and perovskite ($\gamma = 2$) (see text for details). These are lower hemisphere, equal-area projections of (left) the P-wave velocity and (right) the shear wave anisotropy as a function of direction. The plots are in the slab frame, as in Figures 7 and 8 of the main text. For AV_S (shear wave anisotropy), colour shows the strength of splitting in any direction, and black bars show the orientation of the fast shear wave.

Table S1. Upper mantle shear wave splitting corrections used in this study

Station	Longitude (° E)	Latitude (° N)	ϕ (°)	δt (s)	Source
AAM	−83.66	42.30	78.0	1.0	*Fouch et al.* [2000]
AHID	−111.10	42.77	71.6	1.3	*Liu* [2009]
BAR	−116.67	32.68	76.1	1.0	*Liu* [2009]
CCM	−91.24	38.06	31.0	0.8	*Liu* [2009]
CMB	−120.39	38.03	84.0	1.5	*Liu* [2009]
CWC	−118.08	36.44	91.8	1.6	*Liu* [2009]
DGR	−117.01	33.65	94.5	1.3	*Liu* [2009]
DRLN	−57.50	49.26	29.0	0.9	*Barruol et al.* [1997]
DRV	140.00	−66.66	88.0	1.2	*Barruol and Hoffmann* [1999]
EDW2	−117.99	34.88	83.9	1.4	*Liu* [2009]
FFC	−101.98	54.72	45.0	1.0	*Liu* [2009]
FURI	38.68	8.90	36.0	1.4	*Ayele et al.* [2004]
HKT	−95.84	29.96	70.4	1.7	*Liu* [2009]
JCT	−99.80	30.48	30.2	0.5	*Liu* [2009]
L09A	−117.67	42.02	87.0	1.6	*Liu* [2009]
LRAL	−87.00	33.03	65.7	1.1	*Liu* [2009]
MLAC	−118.83	37.63	55.0	1.4	*Liu* [2009]
MNT	−105.38	31.70	33.0	1.1	*Liu* [2009]
NEW	−117.12	48.26	77.9	1.2	*Liu* [2009]
PAL	−73.91	41.01	84.7	1.2	*Liu* [2009]
SCHQ	−66.83	54.83	60.0	1.0	*Niu and Perez* [2004]
SLM	−90.24	38.64	46.7	1.1	*Liu* [2009]
SSPA	−77.89	40.64	67.5	0.9	*Liu* [2009]
TX31	−103.67	29.33	109.0	0.7	*Liu* [2009]
ULM	−95.87	50.25	48.3	1.5	*Liu* [2009]

Table S2. Source-side shear wave splitting results used in the study. Headings are described in the table file `Nowackietal-ts02.txt`.